Designing Plasmonic Sensors to Detect Refractive Index Changes in Palladium

A Thesis
SUBMITTED TO THE FACULTY OF
UNIVERSITY OF MINNESOTA
BY

John Caputo

IN PARTIAL FULFILLMENT OF THE REQUIREMENTS
FOR THE DEGREE OF
MASTER OF SCIENCE

Dr. Vivian Ferry

August 2017

Acknowledgements

I would first would like to thank my advisor Dr. Vivian Ferry. Her passion for this field and strive for excellence has been truly inspiring. She has taught me how to approach scientific problems in ways I would not have thought of. She encouraged me not only to find the answers to scientific problems, but to ask the right questions. These lessons have been invaluable to progressing my research. I greatly appreciate all of her guidance and patience through difficult times. I would also like to thank undergraduate Sihoon Moon for his aid in synthesis, and experiments. He has an exceptional drive and much of this work would not have been possible without his help. He is going to do great things wherever he decides to go. I would also like to thank a number of my group members. Dana Dement for teaching me general lab procedures, helping me take dark-field measurements, taking all the SEM Images, and always being willing to help. She's been incredibly helpful to me and the rest of the lab. I would also like to thank Dr, Mayank Puri. Our discussions on some of the chemical aspects of my project have proved invaluable to my project. He's helped me see things differently and encouraged me to stay positive during periods of slow progress. I'd like to thank Matt Quan teaching me how to use the microscope, and for his in making substrates. I'd like to thank Ryan Connell for his valuable insight in how to run FDTD simulations in practical ways, and different ways to think about my simulations. I'd also like to thank Pavlos Pachidas for showing me the basics of FDTD and for making me laugh. I'd also like thank Ian Slauch for all the invaluable work he's done in improving the gold nanorod synthesis. I'd also like to thank all of my other group members Christian Pinnell, Sydney Jones, and Will Broomhead for all their support and listening to me ramble

on about science. I would also like to thank my committee members for agreeing to serve on my committee, and for all of their great advice over the years. Last, but certainly not least, I'd like to thank my amazing mother. She has always been there to have a late-night pep talk whenever I needed it, and (usually) willing to listen to me babble on about anything and everything. I couldn't have done it without her help.

Dedication

For Mom and Dad, who made me the person I am today.

Abstract

This thesis describes the design and self-assembly of Au nanoparticles to detect hydrogenation in palladium nanoparticles. These gold nanoparticles have a collective oscillation of conduction electrons at a resonant frequency known as a plasmon resonance. At this resonance, a large electric field enhancement occurs that induces a significant increase in scattering intensity. The plasmon resonance frequency is highly dependent on the refractive index of the surrounding medium. Therefore, any change in refractive index of the surrounding will result in a change in peak scattering wavelength. This sensitivity is utilized by dimerizing a palladium nanoparticle with a gold plasmonic nanoparticle. Upon hydrogenation of the palladium, the peak scattering intensity of the plasmonic nanoparticle will shift, effectively acting as a sensor. This thesis describes design considerations when creating a plasmonic sensor. We suggest that the largest change in peak scattering wavelength will likely occur at a wavelength that exhibits the largest refractive index difference between palladium and palladium hydride. Further, we demonstrate an electrostatic self-assembly technique using silicated Au nanorods with Pd nanocubes that showed moderate success. To experimentally investigate the plasmonic resonance location, preliminary dark-field spectroscopy measurements on single gold nanorods were taken. We also describe potential future work opportunities for improvement of self-assembly process and alternative characterization techniques for improved refractive index data.

Table of Contents

List of Figures

1 Introduction

1.1 *Overview*

Although examples of nanotechnology can be found as far back as the 7th century, recent years have seen accelerated research in metallic nanostructures for application in energy, electronics, and medicine.[1] Interest in this research area stems from the unique properties of nanostructured metals relative to their bulk counterparts. Bulk metals are generally size independent and only depend on chemical composition. However, as the metal is reduced in size to the nanoscale, the size and shape of the nanostructure become important, as quantum confinement and Mie scattering dominate the electronic and optical properties.[2,3]

More specifically, when noble metal nanoparticles are reduced in size to the nanoscale, strong absorption and scattering of light occurs via a collective oscillation of conduction electrons known as a localized surface plasmon. At certain frequencies dependent on the shape, size, and electromagnetic environment of the nanoparticle, the localized surface plasmon exhibits a resonance, where the scattering and absorption cross sections may be several times the geometric cross section of the nanoparticle. These localized surface plasmon resonances are directly excitable by incident light. The resonant frequency of plasmonic nanoparticles can be tuned by changing their size, shape, local electromagnetic environment, and proximity to other nearby plasmonic nanoparticles.[4,5] This characteristic means that plasmonic nanostructures with strong light-matter interactions can be designed for a wide range of wavelengths of interest, and that dynamic changes in the optical properties can be introduced via changes in the local environment. This tunability has made plasmonics useful for applications ranging from energy to information technologies, life sciences, and security.[6] Early studies of plasmonics yielded a wide variety of passive plasmonic elements such as mirrors, lenses, waveguides, and resonators, derived from the ability to design nanostructures for specific resonant wavelengths. More recently, active plasmonic nanoparticles and assemblies that change their resonance in response to external stimuli have attracted attention as ways to manipulate light at the nanoscale.[7] This thesis focuses on plasmonic nanoparticles that detect chemical changes in neighboring metallic nanoparticles. Whereas most research in plasmonic sensors has been used to detect changes in dielectric media, as in biosensing applications, active plasmonic nanoparticles that detect changes in nearby lossy or metallic media could be used as switchable mirrors, in data storage, and in monitoring chemical reactions.[8–10]

The goal of this thesis is to design a plasmonic sensor that measures chemical changes in neighboring metallic nanocrystals. Self-assembled dimers of plasmon sensors and catalytic nanoparticles are synthesized, consisting of silica-coated Au nanorods with attached Pd nanocubes. Shifts in the surface plasmon resonance of the Au nanorod are observed at a single particle level upon Pd hydrogenation. This thesis also explores the design principles for plasmonic nanoparticles and assemblies to maximize their sensitivity to chemical changes in Pd nanocrystals.

1.2 Plasmonics Overview

As an incident photon illuminates an individual metallic nanoparticle, the electrons on the surface oscillate in response to the applied electric field of the light wave. This collective oscillation of the conduction electrons occurs at a characteristic frequency, the surface plasmon resonance. As the conduction electrons oscillate, they produce their own electromagnetic field. This produced electric field constructively interferes with the incident electric field to localize the electric field at subwavelength volumes as seen in Fig. 1.[4]

For simplicity, we consider first the general physics behind localized surface plasmons using a simple case of a homogeneous spherical noble metal nanoparticle. Equation 1 describes the polarizability (α) of a spherical nanoparticle assuming the wavelength of light is much larger than the particle diameter (also called the quasistatic approximation). The polarizability is dependent on the electric permittivity of the metal $\varepsilon(\omega)$ and the dielectric permittivity ε_m, and the nanoparticle radius *R*.

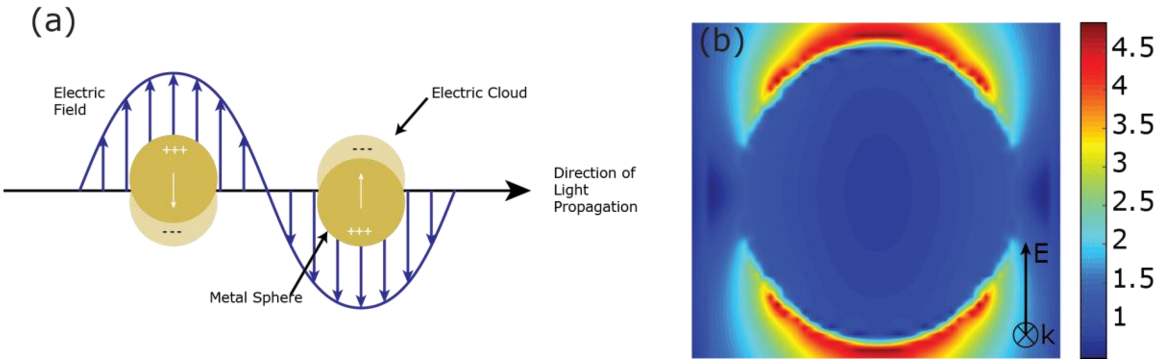

Figure 1: (a) shows reduced scheme of a metal nanoparticle excited at its plasmon resonance. (b) shows electric field enhancement of 60 nm Au sphere at its plasmon resonance of 544 nm

$$\alpha(\omega) = 4\pi R^3 \frac{\epsilon(\omega) - \epsilon_m}{\epsilon(\omega) + 2\epsilon_m} \qquad (1)$$

The polarizability can be defined as the ratio between the net dipole moment induced in the metal nanoparticle and the amplitude of the incident displacement field seen in equation 2.

$$\alpha = \frac{\mu}{\epsilon_0 \epsilon_m \boldsymbol{E_0}} \qquad (2)$$

The polarizability reaches a maximum when $-2\epsilon_m = \epsilon(\omega)$. The frequency where this condition is met is the nanoparticle's plasmon resonance. The scattering and absorption cross sections also depend on the polarizability of the nanoparticle, and therefore on the dielectric function of the surrounding medium. This has profound implications since the plasmon resonance can be tuned by making small changes to the electromagnetic environment of the nanoparticle.[4] For example, if a plasmonic nanoparticle were to be placed in air with a refractive index of 1, followed by water with a refractive index of 1.33, the plasmon resonance will shift to longer wavelengths as shown in Fig. 2.

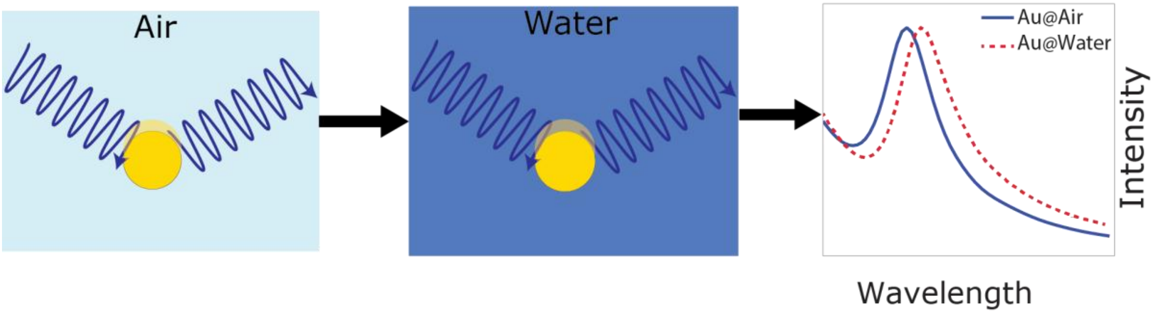

Figure 2: Scheme of submerging Au nanoparticle in air followed by water subsequently redshifts the peak plasmon resonance.[4]

As mentioned, the absorption and scattering cross sections depend on the polarizability of the nanoparticle. The absorption ($\sigma_{absorption}$) and scattering ($\sigma_{scattering}$) cross sections are the ratios of the power scattered or absorbed to the incident power per unit area, and are given in equations 3-4.

$$\sigma_{absorption} = \frac{P_{abs}}{\frac{P_{inc}}{A_{np}}} = \frac{k^4}{6\pi} Im[\alpha] \qquad (3)$$

$$\sigma_{scattering} = \frac{P_{scat}}{\frac{P_{inc}}{A_{np}}} = \frac{k^4}{6\pi} |\alpha|^2 \qquad (4)$$

The cross-section can also be imagined as the area of plane oriented perpendicular to the direction of the incident wave that would intercept the same amount of power that the scattering object radiates.[1]

The plasmon resonance of a nanoparticle can also be tuned by electromagnetic coupling to another nearby plasmonic nanostructure or metal-dielectric interface.[11,12] This coupling could be achieved in a number of ways. For example when two Au spheres are in close proximity, the dipolar plasmon modes hybridize and form two distinct modes with higher and lower energy than the isolated nanoparticles. Another example is the core-shell nanoparticle: by wrapping a metal around a dielectric core, surface plasmons that propagate on the metal-air interface and the metal-dielectric core interface are coupled, further tuning the optical spectrum. Two possible modes are possible due to the different combinations of polarities that the inner and outer plasmon modes can take. Figure 3 shows a silica-core Au-shell (SCGS) for each possible configuration.

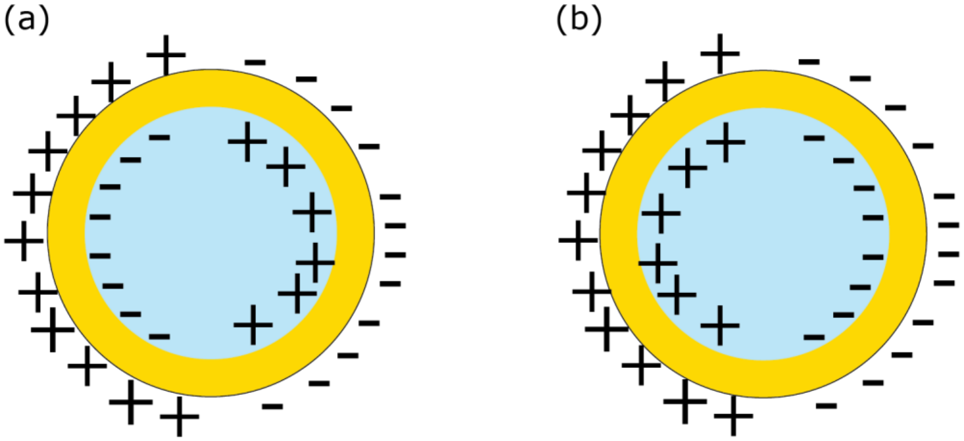

Figure 3 Shows SCGS with polarity of plasmon modes along the inner silica-Au interface and the outer Au-air interface. (a) shows a hybridized mode with polarity opposite the outer plasmon mode. (b) shows a hybridized mode with polarity opposite the outer plasmon mode.

When more complex geometries are introduced, the equations are modified, but still follow similar trends as the simpler spherical geometry. The expression for polarizability along axis *i* of an isotropic, ellipsoidal nanoparticle follows a similar equation as seen in equation 4-5.

.
$$\alpha_i = 4\pi a_1 a_2 a_3 \frac{\epsilon(\omega)-\epsilon_m}{3\epsilon_m+3L_i(\epsilon(\omega)-\epsilon_m)} \tag{4}$$

.
$$L_i = \frac{a_1 a_2 a_3}{2}\int_0^\infty \frac{dq}{\left(a_i^2+q\right)\sqrt{(q+a_1^2)(q+a_2^2)(q+a_3^2)}} \tag{5}$$

The variables a_1, a_2, *and* a_3 all represent the major axis lengths of the ellipsoid axis 1, 2, or 3. L_i defines a geometric factor. Equation 4 demonstrates the versatility of the resonance among different shaped nanoparticles. The plasmonic properties of non-spherical nanoparticles can therefore be tuned in a similar fashion to spherical nanoparticles.[3] Because of this, a wide range of plasmonic nanoparticle shapes can be used to detect changes.[8]

Since the scattering spectrum of plasmonic nanoparticles is sensitive to small variations, ensemble measurements often obscure the characteristics of individual nanoparticles. As the light-matter interaction is strong, the scattering from single metal nanoparticles can be measured using dark-field spectroscopy. Dark-field spectroscopy is similar to conventional transmission optical spectroscopy, except the light is incident at oblique angles, and only the scattered light is collected for measurement. Figure 4 shows a dark field image of Au nanoparticles with a schematic of a transmission-mode dark-field microscopy set-up. The dark-field condenser focuses a light cone on the specimen. Light

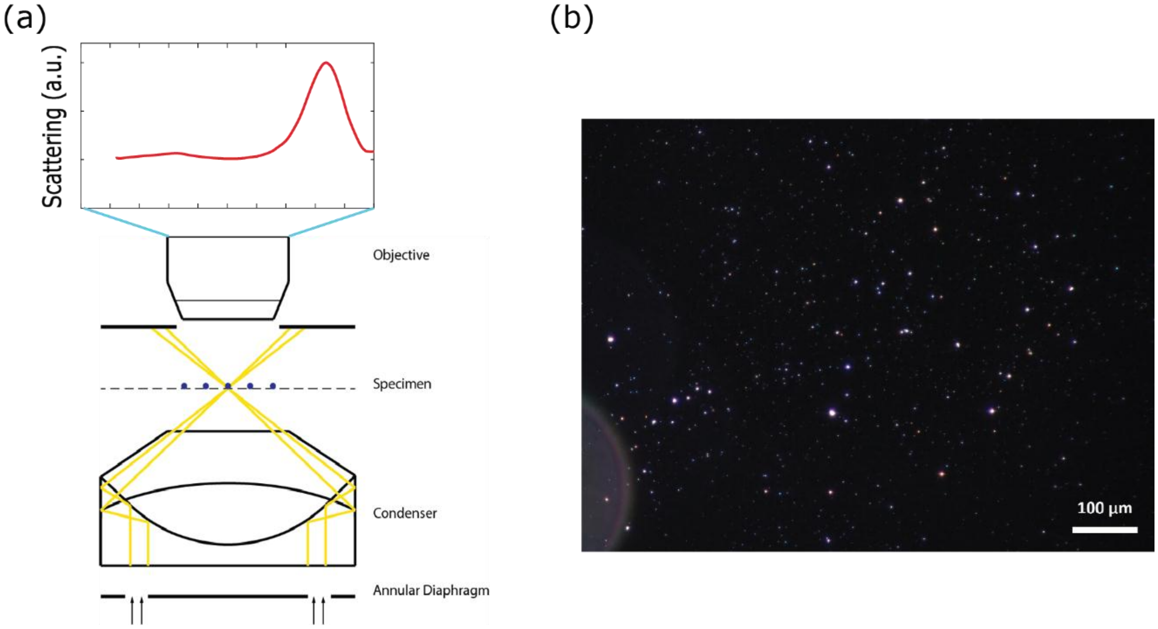

Figure 4: (a) Shows a schematic of a dark-field microscopy set-up resulting in a scattering spectrum of a single Au nanorod. (b) Dark-field microscopy image of 80 nm Au nanorods resonant at approximately 800nm on a silica substrate.

that is directly transmitted through the sample is blocked by the beam-stop, and only scattered light is transmitted. In this way, particles that appear on the substrate are the most prominent while the substrate appears dark. [13] Measurements may be taken in either reflection or transmission mode. The high level of brightness scattering off the nanoparticles seen in Fig. 4(b) is a result of the strong scattering at the plasmon resonance. It is using set-up that we are able to record the spectra of self-assembled plasmonic dimers with Pd nanocubes.

1.3 Creating Plasmonic Sensors

Plasmonic sensors found early application in biological systems, as sensitive methods were needed detect in-situ changes.[14,15] For example, one the earliest applications of this technique was surface plasmon reflectometry. In 1983, Liedberg et al. adsorbed human Immunoglobin G onto a silver surface to detect anti-human Immunoglobin G. As the antibody is passed over the functionalized antigen, a laser is reflected off the surface. As the analyte binds, the surface plasmon resonance on the surface changes causing a deflection in the laser. The extent of the shift could be directly correlated to the concentration of analyte.[16] With the advancement of nanoparticle synthetic techniques, a more sophisticated version of this device was developed by Nath et al. in which a self-assembled monolayer of antigen functionalized Au was bound to a layer of glass. The absorbance spectrum of the Au nanoparticles is then monitored as a function of biomolecular binding of analyte concentration.[17] This technique has the advantage of being implemented with only a UV-V spectrophotometer and has the ability to be modified for a high-throughput assay based screening process.[18]

Since then, research has found different nanoparticle shapes, sizes, and materials that exhibit more dramatic spectral shifts given small refractive index changes.[19] A number of papers have found that anisotropic nanoparticles exhibit superiority to their spherical counterparts.[20] For example, Au nanorods have demonstrated up to 6 times more sensitivity than spherical Au nanoparticles.[21] Au nanostars have shown even greater sensitivity of up to 5 times that of a Au nanorod. This occurs primarily due to the increased electric field enhancement that occurs at the sharp tips.[22]

More recently, plasmonic nanoparticles have been used to detect in-situ changes in metal nanostructures. One of the most common systems is the detection of Pd hydrogenation. As Pd loads with hydrogen, the refractive index changes, which may be detected through a shift in the resonance of a nearby plasmonic nanoparticle. The first example using surface plasmons in detect hydrogenation in Pd was done by Bevenot et al.[23] Pd, followed by silica, and Au were layered around an optical fiber to induce a surface plasmon at the fiber-Au interface. The Pd was then treated with hydrogen to induce a change in the peak transmitted intensity through the optical fiber.[23,24] Tittle et al. later used the concept of monitoring Pd hydrogenation on a Pd film using silicated Au nanospheres.[25] In a similar experiment performed by Langhammer et al., Pd nanoparticles were placed on top of Au nanobars on a glass substrate to measure the thermodynamics and kinetics of Pd hydrogenation. The Au nanobars and Pd nanoparticles were separated by a 10 nm silica spacer layer.[26] One of the earliest instances of performing single particle dark-field spectroscopy to detect chemical changes was done by Liu et al. on an individual Pd disk directly adjacent to a Au nanotriangle.[27]

1.4 Palladium/Palladium-Hydride System

Pd was chosen for these experiments because it is an ideal model system. Improved understanding of Pd hydrogenation is also necessary for application in hydrogen storage,[28] metal-hydride batteries,[29] and switchable mirrors.[9] Upon hydrogenation of Pd, two phases are formed: a hydrogen rich β-phase and hydrogen poor α-phase. Both phases have an FCC crystal structure, the same as the Pd counterpart. As verified by others via neutron diffraction, both phases contain hydrogen occupying random interstitial sites among the FCC lattice as seen in Fig. 5.

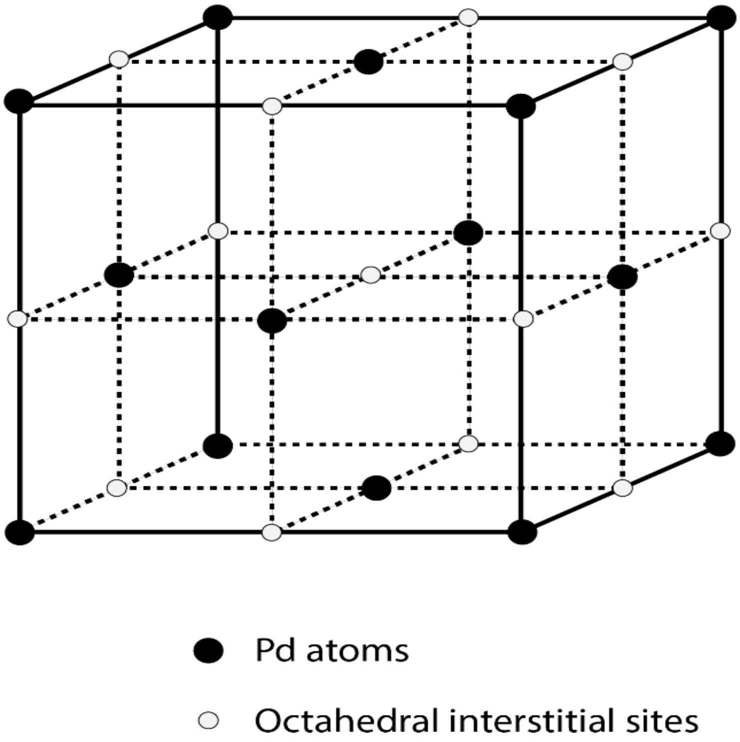

Figure 5: FCC lattice of Pd with hydrogen occupying the octahedral interstitial sites[90]

One major distinction between α, and β phases is the change in lattice constant occurs under hydrogenation. The lattice expansion upon transition from the α-phase to β-phase is approximately 3%. In addition, a smooth transition region from the α to the β phase is present upon Pd hydrogenation, which can be seen as from the plateau in the P vs x diagram seen in Fig. 6. Recent evidence suggests that this transition region disappears in Pd nanoparticles with sizes below 30 nm.[30,31] However, the α-phase and β-phase differ more significantly in their difference in lattice constant.

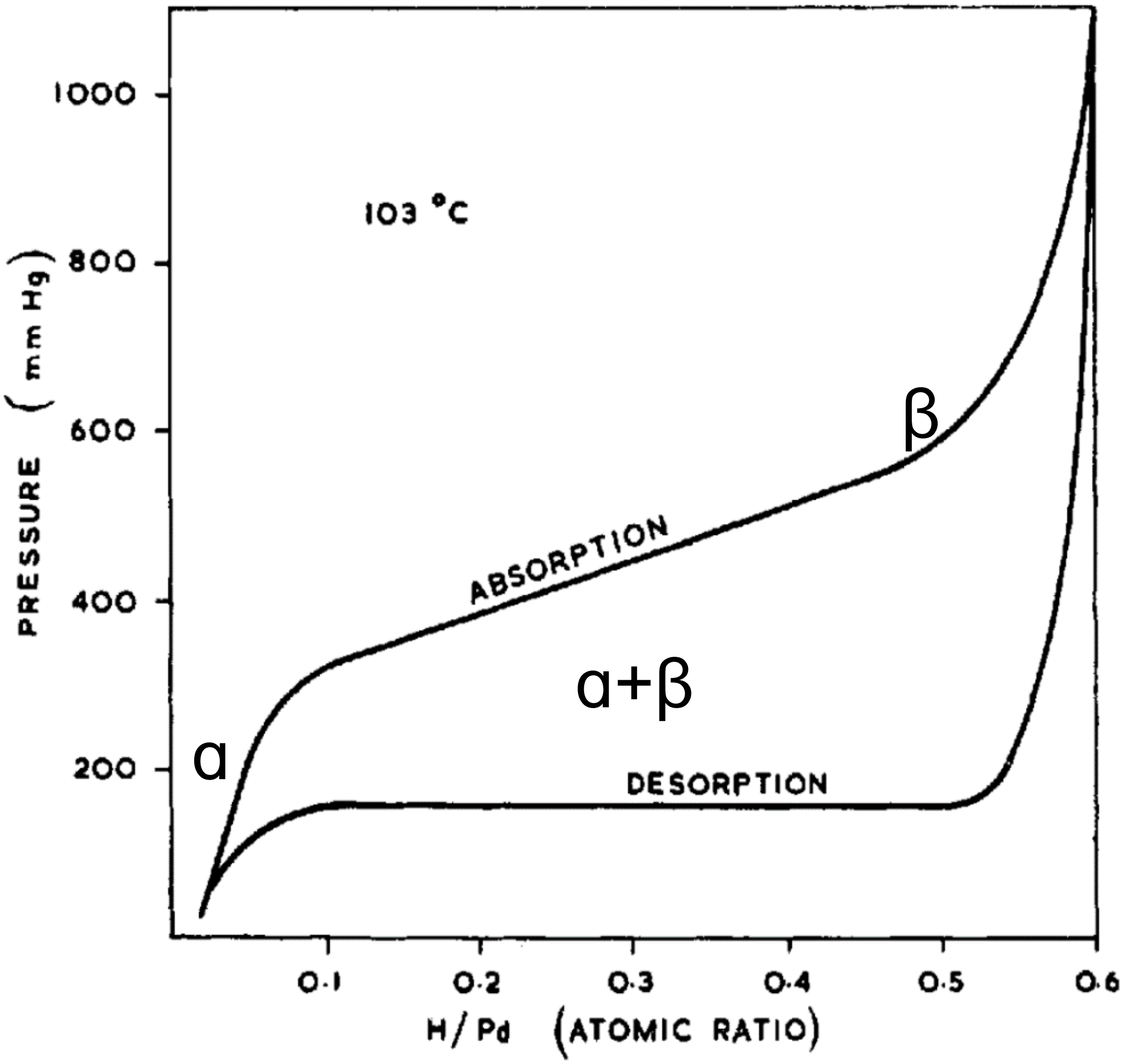

Figure 6: Phase diagram of palladium hydride as a function of atomic ratio hydrogen and Pd.[91] A significant hysteresis is present upon loading and deloading of hydrogen.

As a sensor, one of the key properties is the change in refractive index. Fortunately, the lattice expansion from α-phase to β-phase is accompanied by a large change in refractive index.[32] The refractive index of Pd and PdH at an atomic ratio of x=0.6 are shown in Fig. 7. The difference in refractive index between the two phases is small, but significant.

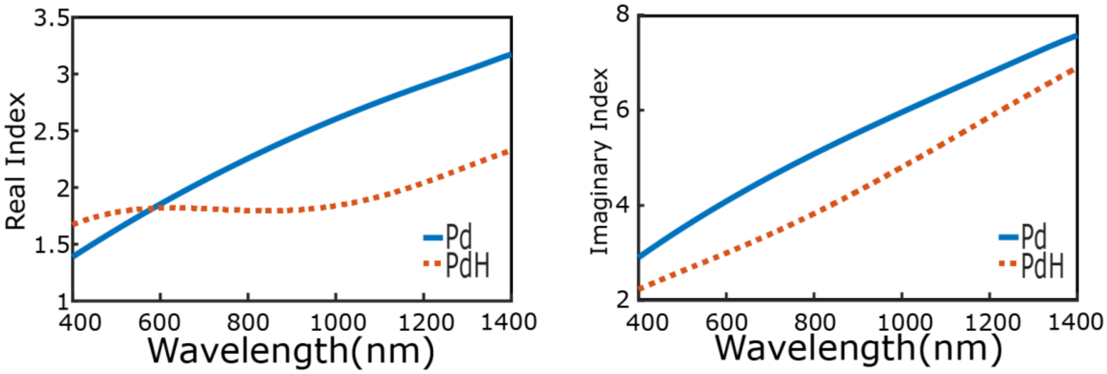

Figure 7: (a) shows the real refractive index of Pd and PdH. (b) shows the imaginary refractive index of palladium and palladium hyride.

The changes between the overall refractive index are enough to induce a change in the surface plasmon resonance in a neighboring plasmonic reporter. Although the real portion of the refractive index of the analyte is most commonly accounted for in plasmonic sensing, the metallic nature of the Pd lends to large absorption losses. This requires considering the extinction contribution to the overall change in refractive index. As such, there will be regions in the visible spectrum that yield a larger difference in refractive index between Pd and PdH. This offers an advantage in that the resonant wavelength of the plasmonic reporter can be tuned to the spectral position in which the largest change in refractive index occurs, to elicit the largest spectral shift upon hydrogenation. This will be discussed in more detail in Chapter 2.

Although some previous work has used plasmonic sensors to detect changes in Pd films, Pd nanocubes have shown to be an interesting point of study from a thermodynamic perspective.[25] For example, Syrenova et al demonstrated that a significant hysteresis between hydrogen loading and unloading pressures exist in Pd cubes. While the loading pressure of hydrogen increases with increasing cube size, no change in unloading pressure occurs.[30] Baldi et al has corroborated this observation and has attributed this behavior surface stress induced from a PdH layer formed at the surface of the Pd cube. Hydrogen atoms saturate the surface of the Pd cube at the grain boundaries, inducing a lattice mismatch between the inner and outer portion of the cube. This surface stress, directly dependent on the cube size, causes differences in diffusion rates of hydrogen through the Pd lattice, causing the difference in hydrogen loading pressure.[31]

1.5 Overview of Thesis

This thesis explores the design and synthesis of self-assembled plasmonic and metal nanoparticles for sensing changes in metallic nanoparticles. We focus on a self-assembled system of Pd nanocubes with silica-coated Au nanorods, and monitor Pd hydrogenation using single-particle dark-field spectroscopy. The optical spectrum is correlated after measurement with the structure using transmission electron microscopy. A spectrum is recorded before and after Pd hydrogenation to study the influence of the extent of hydrogenation on the spectrum of the plasmonic nanoparticle. Chapter 2 will focus on designing the plasmonic reporter not only for Pd, but any material of interest. It will also discussion electromagnetic simulations performed to elucidate the scattering properties of self-assembled systems resonant at different wavelengths. Chapter 3 will discuss the fundamental chemistry behind self-assembly and the rationale behind the self-assembly techniques used in these experiments. Chapter 4 will describe the synthetic procedures for Au nanorods and Pd nanocubes in addition to the self-assembly method. Results and discussion of the self-assembled Au nanorods with Pd nanocubes observed using dark-field microscopy will also be discussed. The conclusion discusses future directions including improvement of current self-assembly methods and the use of other characterization methods.

2 Simulating Plasmonic Sensors

2.1 Sensing Refractive Index Changes with Dispersive Materials

A considerable amount of effort has been devoted to the detection of refractive index changes in dielectric environments via both LSPR and surface-plasmon polariton (SPP) modes on planar metal-dielectric interface. This work includes generating analytical expressions of simple geometry plasmonic sensors, assessing the sensitivity of various different shaped nanoparticles, and using different materials.[33–39] Unfortunately, much of this research cannot be directly applied to this system. The research done in this area has almost exclusively been done to detect changes in a dielectric medium with a constant refractive index.[38] Our system is different in that the plasmonic sensor detects chemical changes in a metal nanostructure (Pd) with chromatic dispersion, or in other words, the refractive index Pd and PdH nanocubes will change with wavelength. Not only is there chromatic dispersion, but that there are also absorption losses associated with Pd/PdH, whereas most literature assumes absorption losses to be 0.[8,33,38] Finally, because the plasmonic sensors are detecting changes in a nearby metallic nanoparticle of finite size, there is a potential of hybridization, whereas the sensors in aforementioned literature cannot hybridize with the subject material, or the dielectric medium. Because of this, a different approach must be taken to understand the behavior of these plasmonic sensors. The following sections describe how plasmonic sensors are designed and can be simulated using full-field simulations to calculate the scattering spectra of all designs.

2.2 *Quantifying Plasmonic Sensor Performance*

While our experimental system is fundamentally different, the basis behind how these sensors are categorized by their performance is worth consideration. The most common way to measure the quality of a plasmonic sensor is by using the refractive index sensitivity factor (RIS), and figure of merit (FOM) as seen in equations.

.
$$RIS = \frac{\Delta\lambda}{\Delta n} \tag{6}$$

.
$$FOM = \frac{\Delta\lambda}{FWHM * \Delta n} \tag{7}$$

$\Delta\lambda$ expresses the change in peak resonance. Δn describes the change in refractive index in the subject material. The FWHM describes the full-width at half-maximum (FWHM) of the resulting spectrum. The RIS of the plasmonic sensor is meant to quantify the sensitivity of the sensor. More abstractly, the plasmonic sensor is more sensitive if a large change in peak resonance occurs given a very small change in refractive index.[35] When observing the scattering spectrum, the resolution of the data is inversely proportional to the FWHM. For this purpose, the RIS is normalized by the FWHM to give the FOM in equation 2. However, there are a few potential drawbacks to using this FOM for a metallic system. The change in refractive index between Pd and PdH is not constant across the electromagnetic spectrum as they are in most biological sensors. This means that Δn may give a misleading value for the figure of merit. For example, if a small change in refractive index Δn were to occur, and a small change in peak resonance occurred, we would likely classify this would not be ideal for our sensor, since we are trying to maximize the change in peak resonance. However, dividing by Δn might increase the FOM giving a false impression of strong performance for this sensor, if the change in refractive is small. For this reason we have introduced a modified figure of merit (MFOM) that normalizes the change in peak resonance only to the FWHM as seen in equation 8. Both the MFOM and FOM should be used to compare plasmonic sensors .

.

$$MFOM = \frac{\Delta\lambda}{FWHM} \tag{8}$$

To design plasmonic sensors for the detection of changes in a dispersive material, the behavior in different regions of the electromagnetic spectrum needs to be explored, as sensitivity of the sensor will be different at different wavelengths. To understand this phenomena, a series of electromagnetic simulations testing two different plasmonic sensors with different Pd cube sizes were tested. Two understand how these simulations were designed, two primary aspects were considered: the scattering cross-section of each nanostructure, and the change in refractive index of Pd

2.3 Scattering Cross Section Considerations

The scattering cross-section of each nanostructure plays a significant role in how the self-assembled Au-Pd dimer’s overall scattering cross-section will behave. For example, the scattering cross-section of an 80nm Pd cube is shown in Fig. 8.

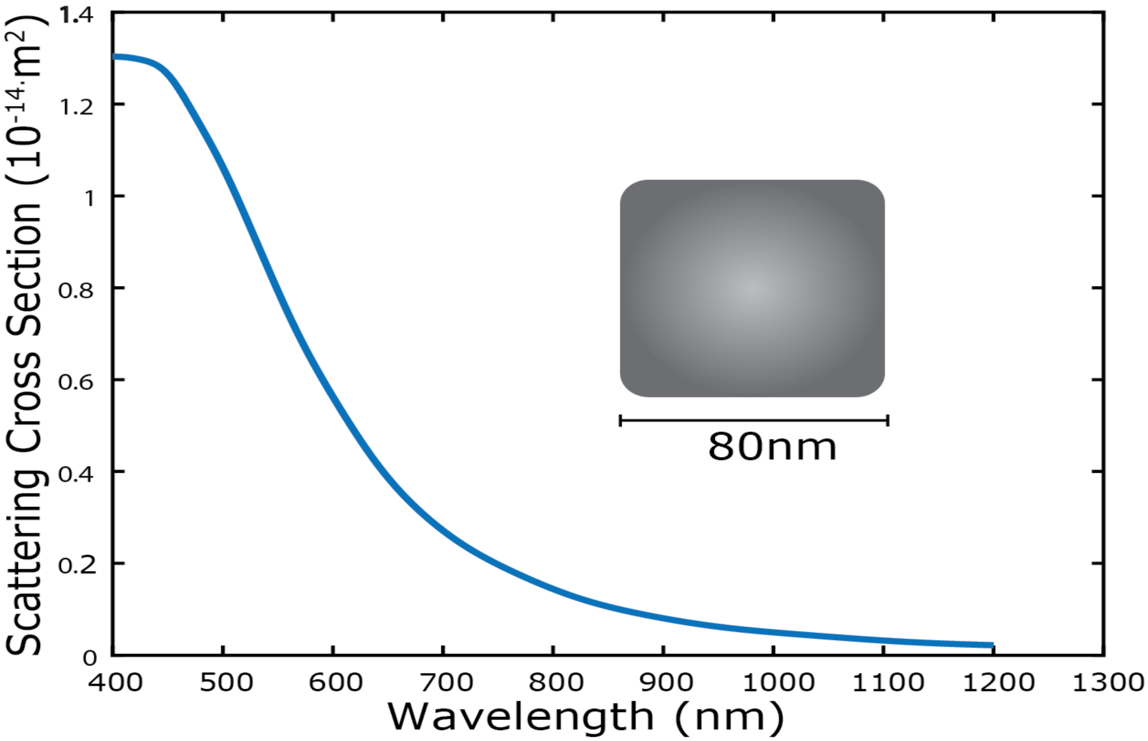

Figure 8: Displays the scattering cross section of an 80nm Pd Cube versus wavelength of incident light.

As shown, the scattering cross-section varies significantly from each end of the spectrum. Given this significant difference, one of the goals of these simulations was to determine the relationship between the scattering cross section of the Pd cube at different ends of the spectrum affects the M/FOM. It has been hypothesized that a large scattering cross-section in the Pd cube, relative to the peak scattering cross section of the plasmonic sensor, may overwhelm the total scattered cross-section of the self-assembled system.

Because the Pd cube has a broad scattering cross-section across the spectrum, this would hypothetically result in a broad scattering cross-section from the self-assembled dimer and a low FOM.

To better compare plasmonic sensors, the scattering cross-section of the plasmonic sensor needs to be fixed when changing the spectral position of the sensor. For this reason, a silica-core Au-shell nanoparticle was chosen to simulate the plasmonic sensors. A silica-Au core shell nanoparticle has an advantage in that the scattering cross section of the sensor can be tuned independently of the peak spectral position. This is done by changing the core size and the shell thickness simultaneously. This ensures that when comparing different plasmonic sensors with the same size Pd cubes, the scattering cross-section of the sensors will be the same, and the differences in the FOM will not be skewed by having one sensor's scattering cross section larger than the other. Using the quasistatic approximation, a scattering spectrum based on core and shell sizes along with refractive index data can be

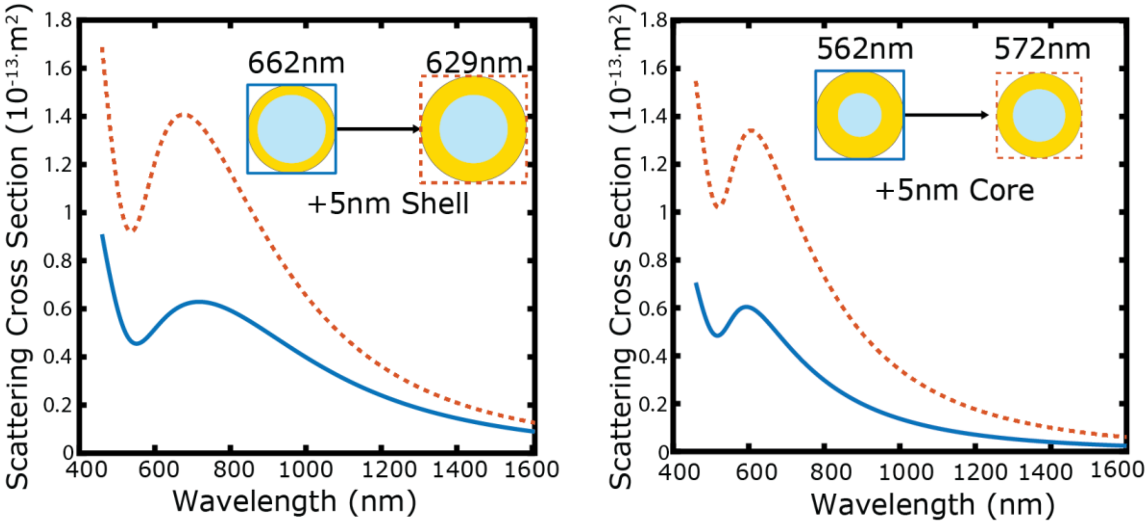

Figure 9: (a) shows a SCGS of core size diameter of 100nm and shell thickness 5nm increasing to a thickness of 8nm with the same core size with the corresponding scattering spectrum in red and blue. (b) shows a SCGS of core size diameter of 50nm and shell thickness 20nm increasing to a thickness of 25nm with the same shell with the corresponding scattering spectrum in straight and dashed lines. The peak resonance of each size is listed above diagrams.

calculated as demonstrated in Fig. 9.[3] Based on using the approximation, we were able to estimate sizes that would be needed maintain scattering cross-section while changing peak resonance. We then simulated the full-field solution using the finite difference time domain (FDTD) method (Lumerical FDTD Solutions). The dimensions and scattering cross section of plasmonic sensors designated Sensor A and Sensor B are shown in Fig. 10. The full-width half maxima of the two sensors are also similar, within 20% of each other.

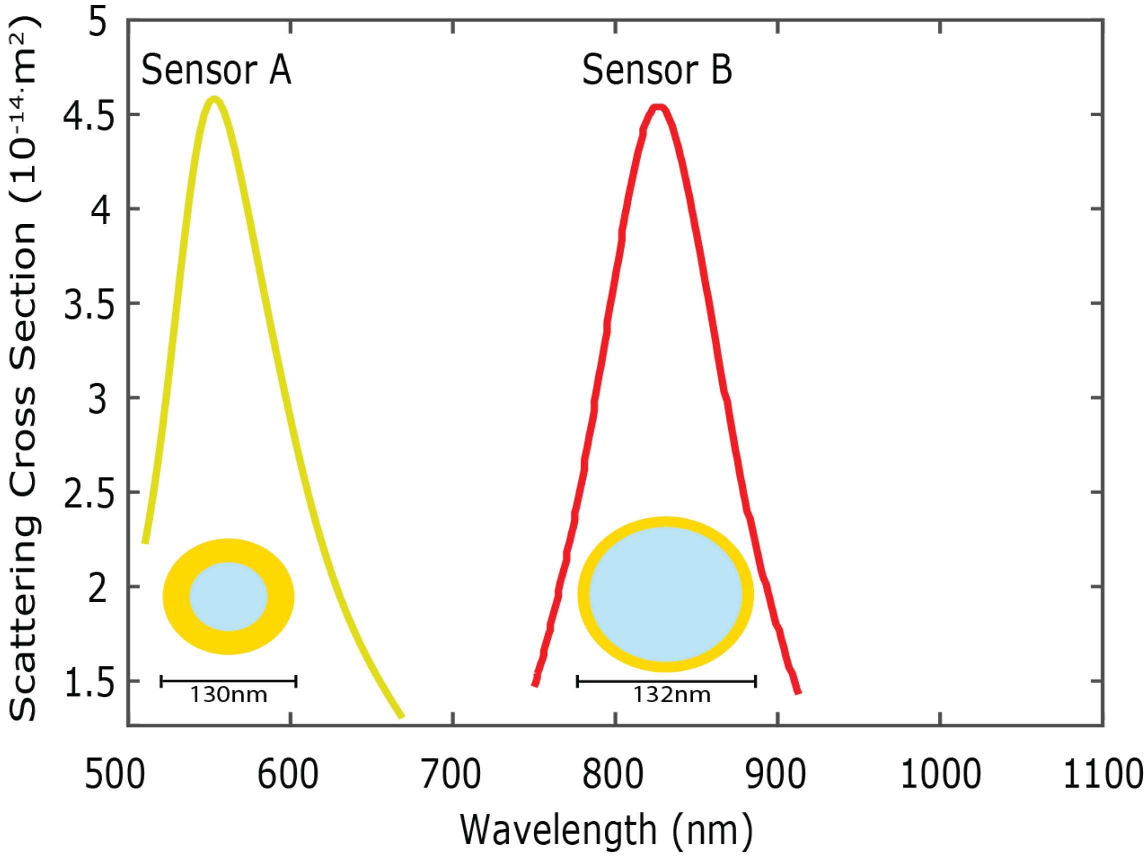

Figure 10: Shows the dimensions of Sensor A and Sensor B with their corresponding scattering spectra.

2.4 Refractive Index Considerations

The other primary consideration is the refractive index of the Pd cube. There are certain wavelengths in the electromagnetic spectrum that will have a larger change in refractive index from Pd to PdH than others due to chromatic dispersion.[40] Therefore, another goal of performing these simulations was to determine if tuning the peak resonance of the plasmonic sensor to a wavelength with a larger Pd-PdH refractive index change would increase the spectral shift in peak plasmon resonance. Figure 11 displays the change in refractive index from palladium to palladium hydride for a 10 nm Pd thin film fitted using the Lorentz-Drude Debye Model.[40,41] Unlike the plasmonic sensors described in the

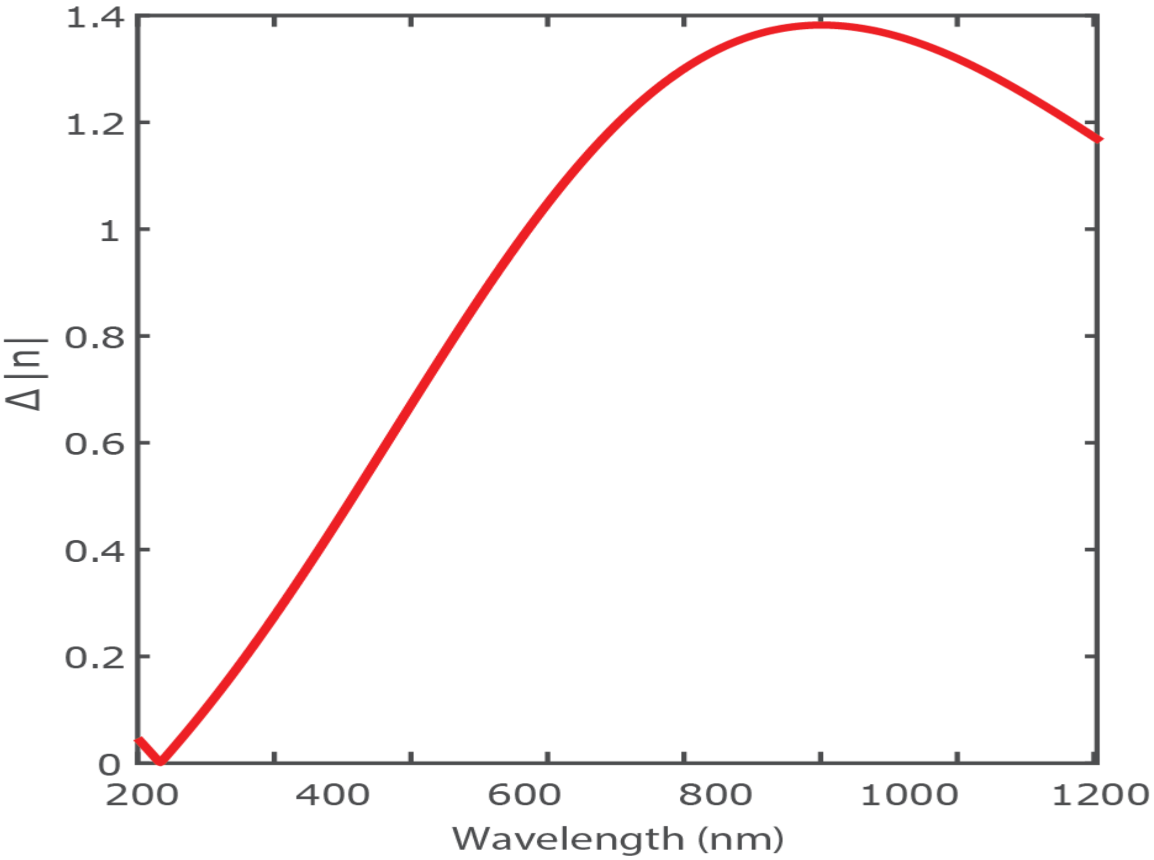

Figure 11: Difference in magnitude of refractive index from Pd to PdH vs wavelength.

aforementioned literature, the change in refractive index is calculated to include the extinction coefficient. The magnitude of the refractive index is calculated using the complex conjugate of the real and non-real coefficients.

Based on Fig. 11, the maximum change in refractive index occurs around 900 nm, indicating a plasmonic sensor with a peak resonance closer to 900 nm may elicit a greater change in peak resonance. To test this, the sizes of sensor A and sensor B were chosen not only to match scattering cross-section, but also to place their peak resonance where the change in Pd refractive index was significantly different. Sensor A was chosen to be resonant near 550 nm, corresponding to a net change of approximately 0.6 nm in refractive index. The sensor B was chosen to be resonant near 850 nm with a net change of approximately 1.35 in refractive index. This can be seen more clearly in Fig. 10.

2.5 *Simulation of Plasmonic Sensors*

The plasmonic sensors can be simulated using a FDTD solver of Maxwell's equations.[42] Each plasmonic sensor was tested using the same set of sizes of Pd cubes and the same gap distance of 5nm. This gap distance ensures that the Pd cube is sufficiently close to the plasmonic sensor to ensure a strong shift in peak resonance, but isn't excessively computationally intensive. The simulation has the plasmonic sensor placed with a palladium cube on a thick silica substrate. A sample scheme is seen in Fig. 12.

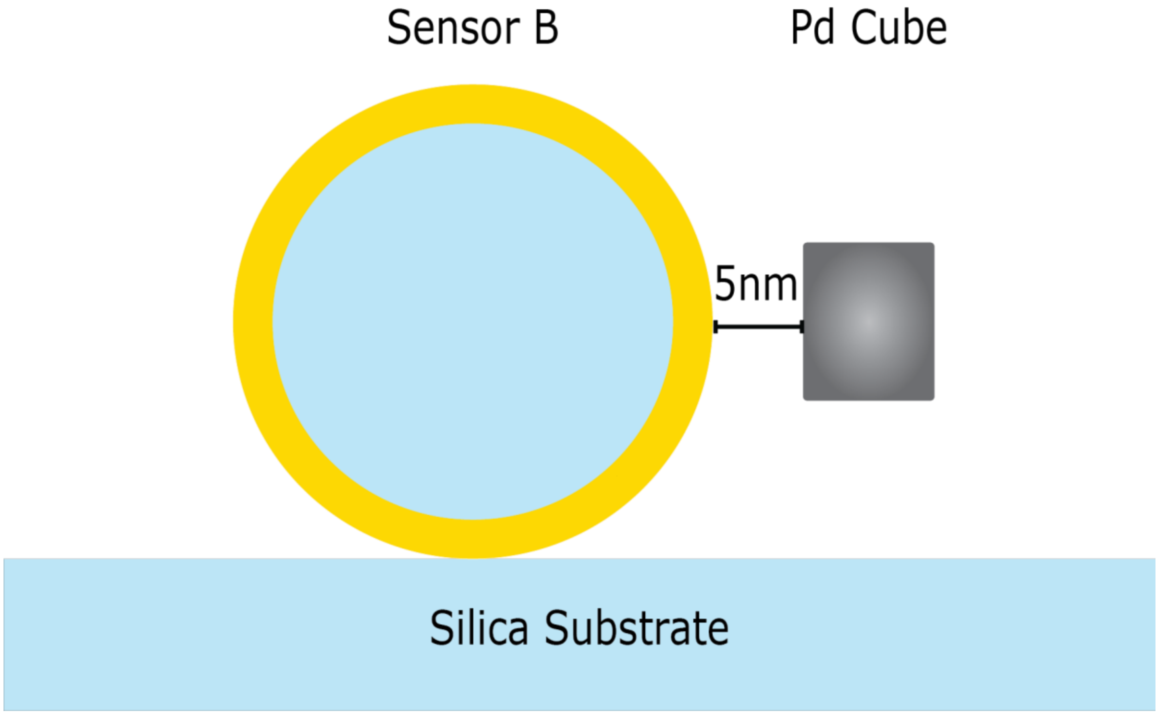

Figure 12: Scheme of Sensor B with a Pd cube as is simulated to be simulated Lumerical ®.[42]

Ultimately, these simulations will provide help determine the sensitivity of plasmonic sensors at different wavelengths without having to synthesize perform an equivalent experiment in the laboratory. Due to limited resources, we were unable to perform the simulations to completion, but the fundamentals behind these simulations have been established and can be applied to future work.

3 Self-Assembly and Synthesis

3.1 *Approaching Self-Assembly*

The bridging of colloidal nanoparticles through non-chemical bonds is known as self-assembly.[43] There are many different possible chemicals that can link colloidal nanoparticles, including DNA, proteins, polymers, and lipid vesicles.[44–46] To choose the self-assembly method, various aspects of the assembled nanoparticles can be considered such as the required interparticle spacing, the surface functionalization, the shape, and the orientation. The orientation of the self-assembled dimer is of less importance in our case, as our experiments utilize single-particle spectroscopy to take measurements. Any inconsistencies in the orientation of the self-assembled nanoparticles can be accounted for. Interparticle spacing is the most important factor: the Pd nanocube must be within a certain distance of the plasmonic sensor, determined by the decay length of the electric field away from the interface, or no response will be detected. Preliminary simulations suggest that as the Pd nanoparticle is brought closer to a plasmonic sensor, the electromagnetic coupling increases and the resonance shifts further (see SI Table 1).

Therefore, minimizing the distance between the particles as much as possible is the key characteristic to consider when choosing a self-assembly technique. With many options for self-assembly techniques that could be applied to achieve a small gap distance, we would like to use a technique that achieves self-assembly with as few steps as possible. DNA-directed self-assembly, while powerful, requires a number of functionalization and purification steps using gel electrophoresis to create nanoparticle dimers.[47] In addition, the vast majority of DNA self-assembly has been applied toward homodimers or two nanoparticles consisting of the same material, or to large area crystals.[48–51] Our experiments require the assembly of Au nanoparticles with Pd nanocubes as heterodimers. We chose to use an electrostatic self-assembly method. While a number of groups have had success with creating heterodimers, Gschneidtner et al. has adapted an electrostatic self-assembly for dimerization of heterodimers that has been modified for use with our nanoparticles. Their self-assembly method allows heterogeneous nanoparticles to be self-assembled with distances as short as 0.9 nm. Their technique only involves surface modification of the nanoparticles to induce self-assembly.[52] Due to all these benefits, their electrostatic self-assembly method was adapted for use with silicated Au nanorods and Pd nanocubes.

3.2 Electrostatic Self-Assembly

Electrostatic self-assembly uses electrostatic attraction of oppositely charged surfaces to self-assemble nanoparticles. In order to describe electrostatic self-assembly, a few basic concepts in surface and colloid science are needed. Figure 13 shows a model for the ion arrangement on a colloidal nanoparticle surface with relevant locations depicted. The stern layer is defined as the width of the region with oppositely charged bound counterions to the colloid surface. Beyond this layer, a diffuse layer of charged particles is in continuous thermal motion close to the surface of the colloid. This diffuse layer can undergo tangential stress from the surrounding fluid. The plane that separates the mobile fluid in the bulk from the fluid that remains close the colloid surface is known as the slipping plane.[53–55]

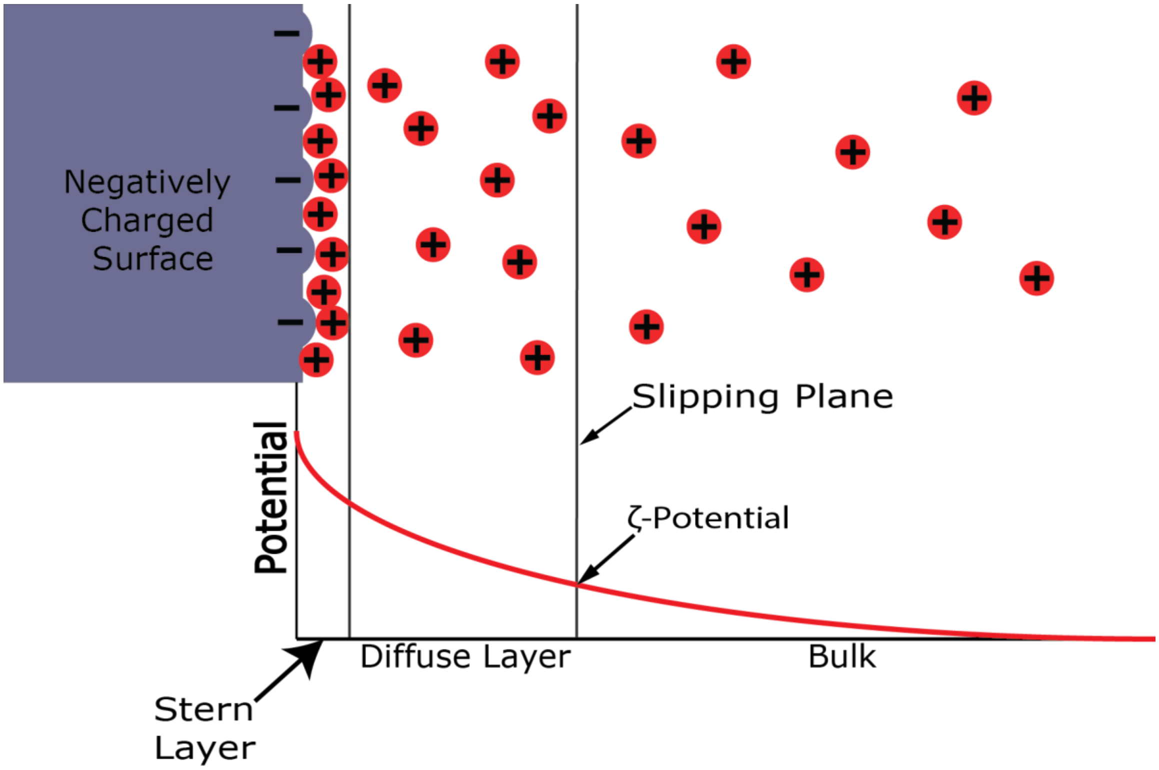

Figure 13: Shows a negatively charge surface in water with physioadsorbed counterions on the surface in the stern layer. The counterions have much more space with rapid thermal motion in the diffuse layer. The layer separating the diffuse layer and the bulk solution is the slipping plane. The potential at the slipping plane is defined as the zeta-potential.[92]

The most important feature of this model is the zeta potential. The zeta potential is defined as the electrostatic potential difference between the interface of the slip plane and the bulk medium. When particles with zeta-potentials of opposite sign come in close proximity, they attract one another. For example, Gschneidtner et al. used Au nanospheres functionalized with the negatively charged ligand 2-mercaptoethanesulfonate (MESNa) to self-assemble with Pd cubes functionalized with the positively charged surfactant cetrimonium bromide (CTAB).[52] Using this same idea, we can functionalize our Au nanorods and Pd nanocubes with oppositely charged ligands to induce dimerization.

3.3 Au Nanorod Synthesis

As a proof of concept for heterogeneous nanoparticle self-assembly, Au nanorods were chosen as the plasmonic sensor to be self-assembled with Pd cubes. Au nanorods were chosen as the plasmonic sensor for two primary reasons: the synthetic versatility and sensitivity. The Au nanorod syntheses that we utilized have the advantage being more easily tunable and more monodisperse than previously reported nanorod synthesis.[56,57] In terms of sensitivity, the Au nanorods also have a narrower FWHM in the near-infrared than Au spheres. [58]

The Au nanorods are synthesized using a seeded growth process. The seeded-growth method is the most widely used method to synthesize Au nanorods.[59] Seeded-growth synthesis has the advantage of separating the nucleation and the growth stage of the Au nanorods. This gives much greater control over the size and dispersity of the nanorods.[60] It is crucial that all water is Millipore grade water (referred to as MH_2O). The seeds are synthesized in a growth solution of 5ml of 0.5mM $HAuCl_4$, and 5 ml of 0.2M CTAB solution. Subsequently, 1 ml of 1mM $NaBH_4$ is added. The $NaBH_4$ reduces Au^{3+} in solution into Au^0 to Au seeds. The CTAB in solution forms a micelle around the Au seeds acting as a template for the Au nanorod growth. In a separate beaker, a growth solution of 7 grams of CTAB, 1.234g of Sodium Oleate, in 250 ml is added to 250ml of 1.0 mM $HAuCl_4$ bringing the total volume 0.5L. The Sodium Oleate acts a secondary reducing agent to reduce Au^{3+} to Au^+. This secondary reduction allows for a wider range of nanorod sizes to be produced and allows for much more uniform Au nanorods. After the system has equilibrated, 24 ml of 4mM silver nitrate solution is added. The silver nitrate is a major component ensuring anisotropic growth of the Au nanorods. The mechanism for Ag participation in the anisotropic growth is not completely understood, and multiple mechanisms have been proposed.[61] However, the strongest argument appears to be that a Ag-Br-CTA complex forms and adsorbs preferentially onto the longitudinal faces, thus allowing the growth rate to be faster on the ends of the rod and slower on the sides.[62] After

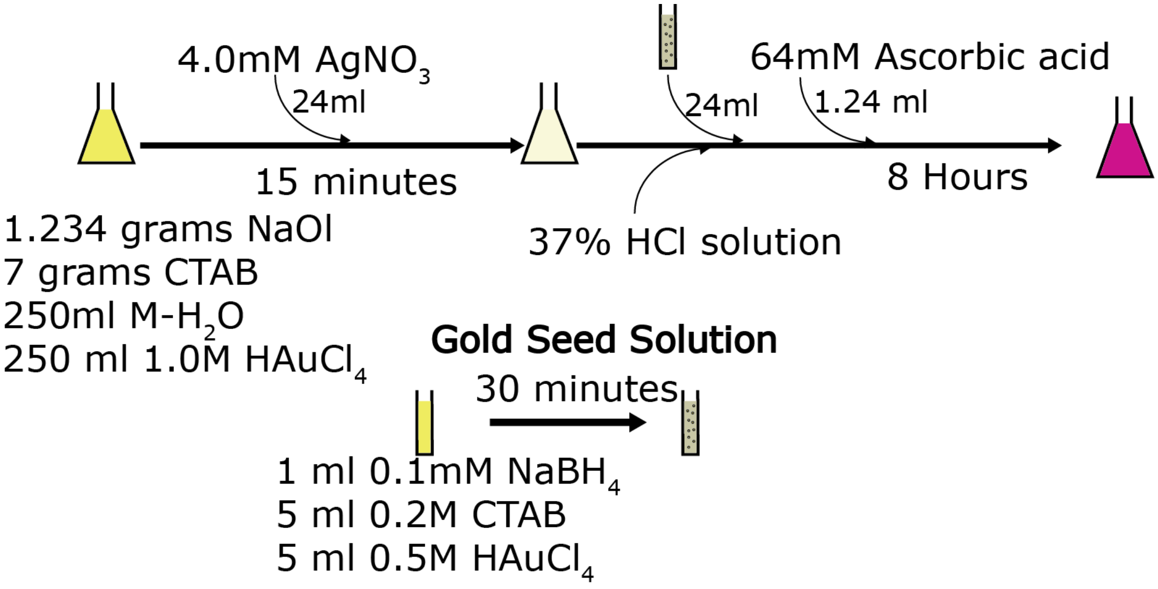

Figure 14: Au nanorod synthesis scheme produced using method by Ye et al.[56]

the $AgNO_3$ has equilibrated after 15 minutes, 1.5ml of 37% spectroscopic grade HCl is added to adjust the pH. Following this step 0.2 ml of the aged seed solution is added to the growth solution followed by 1.25 ml of 0.064 M L-ascorbic acid is added to the solution. The L-ascorbic acid reduces the Au^+ to Au^0 to form Au nanorods. The beaker is stirred rigorously for 30 seconds and stopped. The beaker is left overnight for 8 hours. The synthesis scheme is represented graphically in Fig. 14.

After synthesis, centrifuging the sample to remove the majority of the CTAB ligand is crucial for easy visibility under the TEM and for controlling the extent of silication. The final concentration after centrifuging is less important than the consistency of centrifugation. If different batches of Au nanorods are synthesized at different times, it is imperative that the CTAB concentration be as consistent as possible between batches. After synthesis of Au nanorods, the solution is separated into 50ml centrifuge tubes. The samples are centrifuged at 8000x*g* at 45 minutes. After the solution has separated, the supernatant is decanted until less than 3 ml of Au nanorod solution is present at the bottom of the centrifuge tube. An equal amount of Millipore water is used to replace the supernatant. The cycle is repeated one more time. On the second cycle, instead of replacing the entire supernatant volume of water, the sample is poured into one centrifuge tube to combine all Au nanorod samples into one concentrated sample. After the Au nanorod sample is poured into the concentrated sample, the Au nanorod sample container is rinsed with exactly 2 mL of Millipore water to rinse off any residual Au nanorods off the container. After rinsing the container, the rinse is also poured into the concentrated container. This rinse process only applies to the Ye et al.'s synthesis in preparation for silication discussed in the next section.[56]

The procedure developed by Kozek et al. is very similar to the procedure developed by Ye et al., but with two minor differences: the Kozek synthesis does not use sodium oleate, and a solution of KBr is also added to the growth solution. In the Kozek procedure, the seeds are synthesized in a growth solution containing 1ml of 2.94mM $HAuCl_4$, 5 ml of 0.125 M CTAB solution by adding 0.6 ml of 1.11mM $NaBH_4$. In a 1L media bottle, a growth solution of, 770ml of 122mM CTAB, in 200ml of 0.481mM $HAuCl_4$, 10ml 94.1mM KBr, 10ml 1.92mM AgNO3 solution, 1.358 ml of seeds, and 10ml of 10.5mM L-ascorbic acid bringing the total volume approximately 1L. This sample was placed in a water batch at 30C for 1 hour. A secondary reduction solution of L-ascorbic acid as added after the 1 hour water bath. 50ml of 9.48mM L-ascorbic acid over a period of 171.4 minutes. A scheme of this synthesis is shown in Fig 15.

After this period, the Au nanorod growth is finished and ready for centrifuging. The Au nanorods are split into 50 ml centrifuge tubes in 30 mL aliquots. The samples are centrifuged at 10,000x for 20 minutes. After centrifugation, 29 ml of supernatant is removed via pipet. The 29ml is replaced with M-H2O. This sample is centrifuged again and 29ml of supernatant is removed. 2ml of MH2O is added to the sample. The samples are pipetted into one concentrated stock solution.

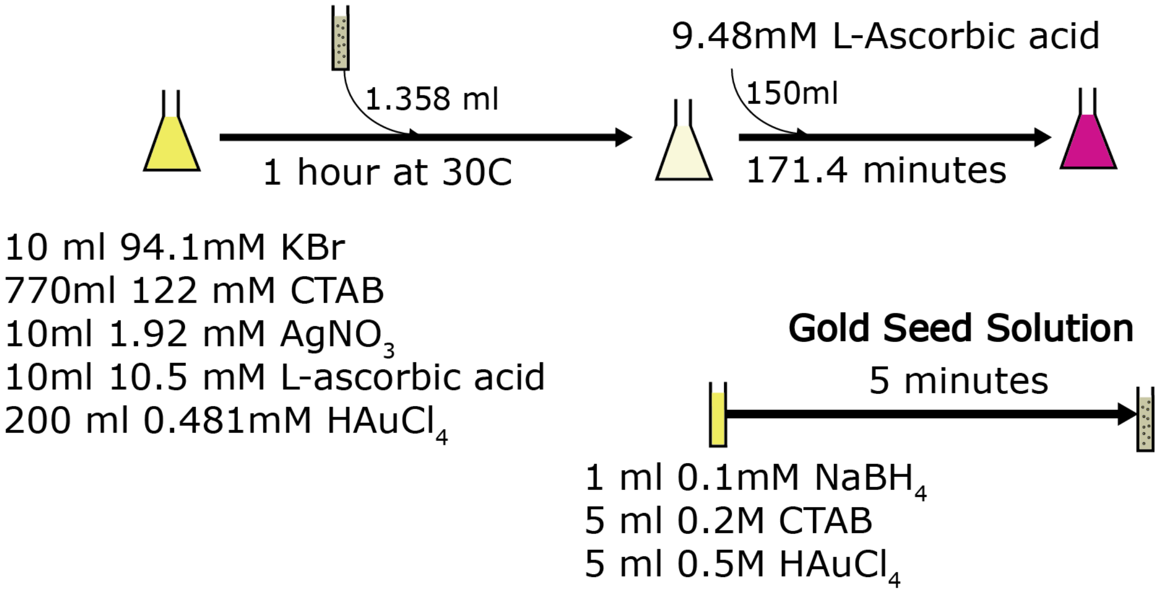

Figure 15: Au nanorod synthesis scheme produced using method by Kozek et al.[57]

An important aspect in preparing the UV-VIS sample is the dilution. Because the Au nanorods, have extremely high absorbance after concentrating, a small amount of sample must be diluted to obtain an accurate UV-VIS sample. Typical dilutions were 300uL of sample in 10ml of water. Care needs to be taken at this stage as the CTAB concentration will be very low after dilution. If too much time is allowed to pass, the Au nanorod solution can aggregate. It is best to perform dilution quickly and take a UV-VIS sample. Taking a UV-VIS is not only important to determine the peak resonance of the Au

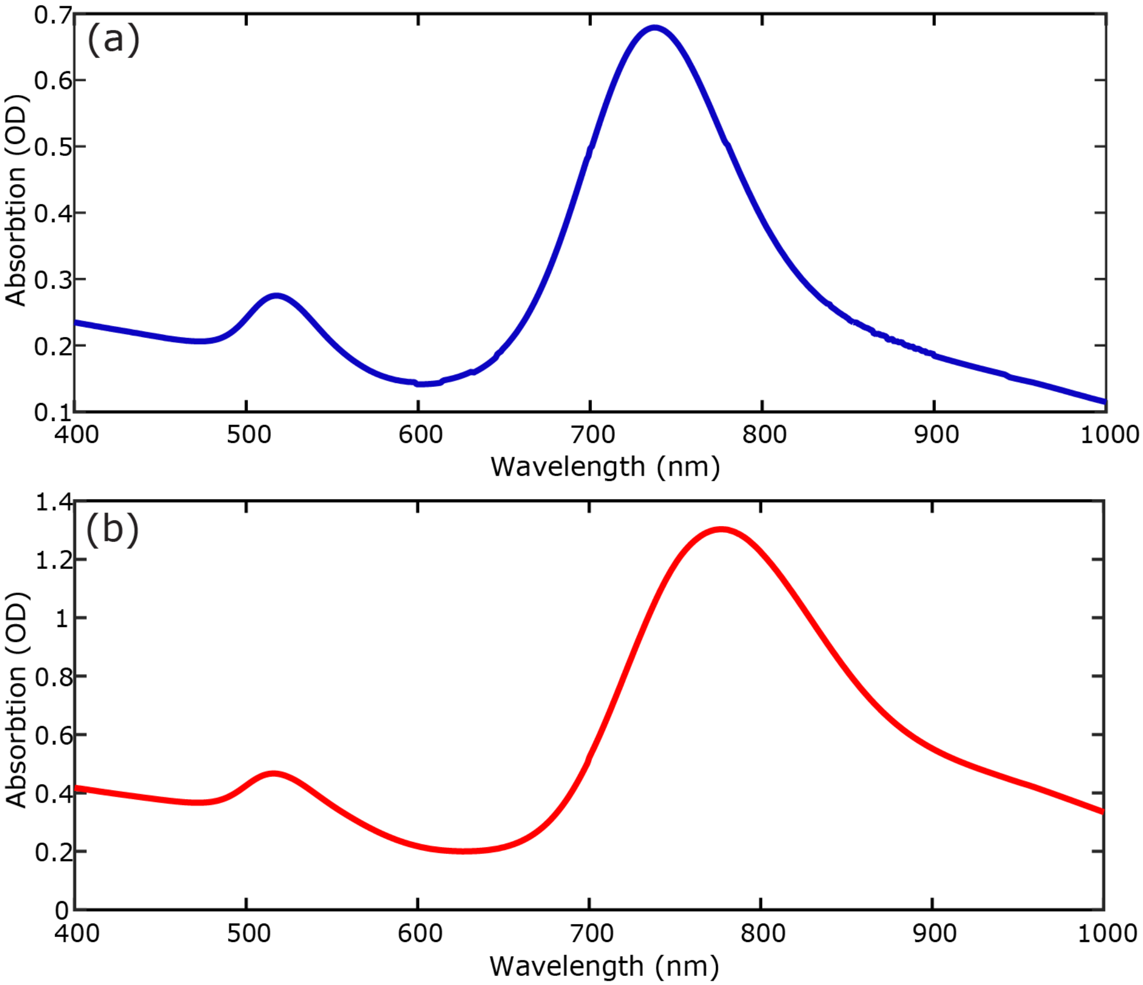

Figure 16: (a) UV-VIS absorption spectrum of Au nanorods synthesized using the procedure by Ye et al. resonant at 738nm. UV-VIS absorption spectrum of Au nanorods synthesized using the procedure by Kelev et al. resonant at 778nm.

nanorods, but also to determine their final concentration. By knowing the peak absorbance of the diluted solution, the peak absorbance can be closely estimated assuming Beer's law with a linear dependence on absorption and concentration.[63] The absorbance at 400 nm should be used to calculate the absorbance of the stock solution. Using the absorbance at 400 nm will ensure that concentration between different Au nanorod stocks will be consistent if their aspect ratios are different.[64] The UV-VIS of Au nanorods synthesized following the procedure developed by Ye et al. and Kozek et al. are shown in Fig. 16.

3.4 Formation of Silica Layer: Ye Synthesis

. Recent evidence suggests that at close spacing of Au and Pd, interdiffsuion of materials may occur.[65] A later study by Tittl et al. demonstrated that introducing a silica barrier between Au and a Pd film isolates Au from interdiffusion.[25] For this reason, a layer of silica is coated on the Au nanorod surface. This likely prevents any potential interdiffusion of neighboring Au/Pd nanoparticles that could alter the optical response of the dimer.

We used a method to form a mesoporous layer of silica around the Au nanorods that was pioneered by Gorelikov and Matsuura, but has been modified to reduce reaction time and decrease thickness.[66,67] The synthesis is a base catalyzed sol-gel synthesis with Tetra-ethyl orthosillicate (TEOS) hydrolyzing to form an amorphous silica shell around a CTAB functionalized Au nanorod[66]. Figure 17 shows a simplified schematic of this process.

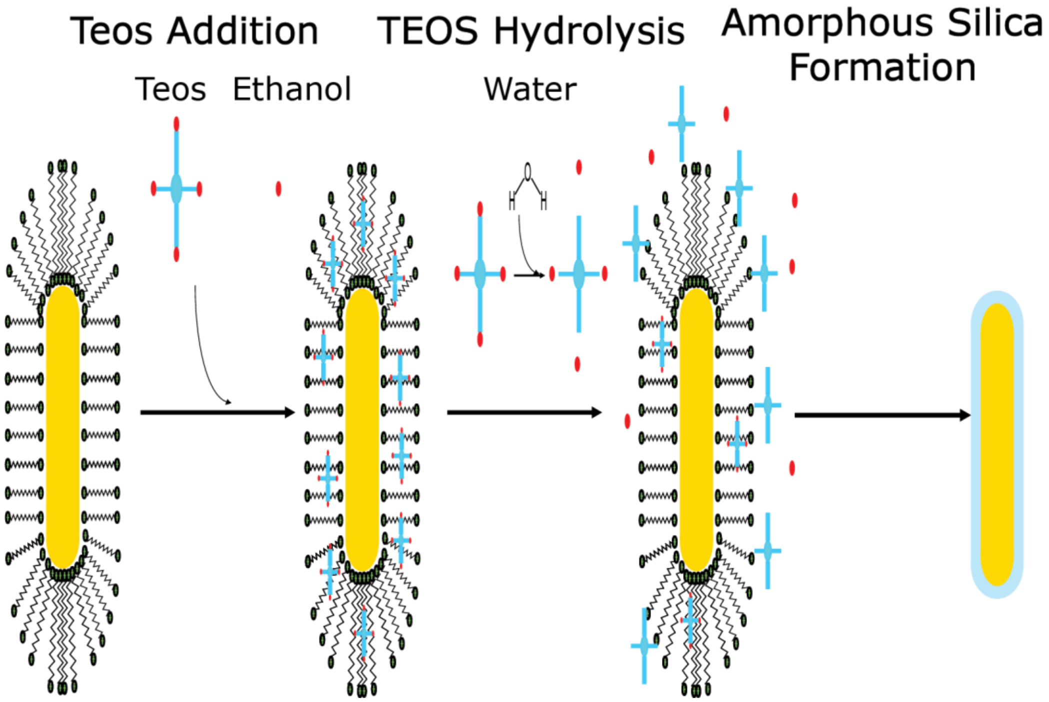

Figure 17: Simplified scheme of a CTAB functionalized Au nanorod treated with TEOS and Ethanol to undergo base-catalyzed hydrolysis. Base species omitted for simplicity; figure was adapted from graphic depiction listed in Ye et al.[93] The CTAB micelle layer is omitted on the last step for clarity.

The Au nanorod silication done with Ye et al.'s procedure was done on a 10 ml scale. This was to ensure that Au nanorod solution wasn't used excessively and could be used consistently in many samples. When performing experiments on a small scale, extra care needs to be taken to ensure CTAB, ethanol, and water concentration is consistent because of this, stock solutions of CTAB and EtOH/Water were used for all samples. A stock solution of CTAB in a solvent of 2:1 Water/Ethanol by volume was used at a concentration of 0.164M. 2.276 ml of the large stock solution and 11.057 ml of EtOH/Water stock are administered into a 20ml scintillation. This creates a second stock solution at 28mM. Finally, 1ml of this second stock solution is added to 9 ml of the EtOH/Water stock solution in a separate 20 ml scintillation vial. After slightly shaking solution, the required amount of Au nanorods is added to the solution. The Au volume added is based on the desired final absorbance of the solution We found a final absorption of Au nanorods in silication solution is adequate at an absorbance of 0.2805 at 400 nm (typically around 0.4ml of concentrated Au nanorod solution). This absorbance ensures the formation of empty silica spheres is minimal.

After adding the Au nanorods into solution, at least 1 hour is allowed to ensure equilibration of rods and CTAB stock solution. After that 15ml of 38% NH_4OH is added to change the pH to ~10. After that, 3.3 uL of TEOS is added to adjust the stock concentration to 1.3mM. The solution is rigorously stirred for 2 minutes and left undisturbed for another 30 minutes. After the 30 minutes, 40uL of 2 -[methoxy(polyethylene-oxy)9-12propyl]trimethoxysilane (PEG-s) is added. The solution is stirred rigorously for 2 minutes and then left undisturbed for 20 hours. Following silication it is important to centrifuge completed sample as the silica shell can continue to grow if left for multiple days. A scheme for this procedure is shown in Fig. 18.

Our preliminary simulations of silica-core Au-shell and Pd cube dimers suggested a gap distance of 5 nm was a sufficiently small distance to detect a shift in the plasmon

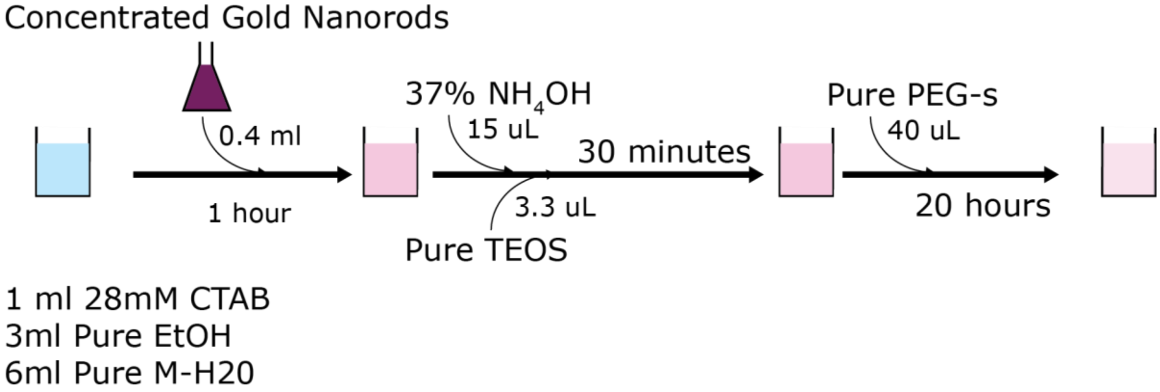

Figure 18: Silication procedure developed by Ye et al.[67]

resonance (See SI Table 1). With this in mind, the silica shelling procedure was designed to achieve a silica shell thickness under 5 nm to minimize the distance between the attached Pd nanoparticle and the Au nanorod. By taking the shelling procedure used by Nguyen et al., we determined a minimum thickness of approximately 15 nm was achievable by lowering the TEOS concentration from the literature concentration of 1.5 mM to 1.3 mM.[67] Any concentration lower than 1.3 mM resulted inconsistent coating of the Au nanorod. Figure 19 shows the results of using a TEOS concentration of 1.3 mM followed 1.15 mM.

To achieve thinner shells, we introduced a terminating ligand. Wu et al. demonstrated a modified silication method that introduced 2–[methoxy(polyethyleneoxy)9 ‐12propyl]trimethoxysilane (PEG-silane) during the synthesis to terminate the growth prematurely.[68] By introducing PEG-s 30 minutes after administration of TEOS at 1.5 mM, we were able to synthesize a 10ml solution silicated Au nanorods with a thickness of 5nm as seen in Fig. 19.

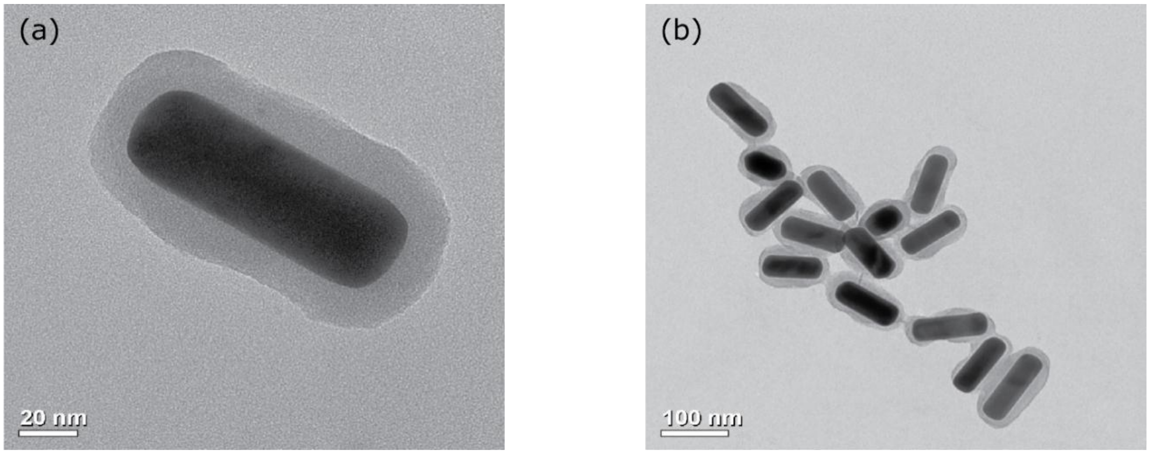

Figure 19: (a) shows a TEM image of a conformal silica coating around Au nanorod treated with TEOS at a concentration of 1.5mM. (b) shows the same Au nanorods with non-conformal coatings of silica around the Au nanorods treated with TEOS at a concentration of 1.3 mM.

While initial attempts proved promising, consistent shell thickness under these experimental conditions could not be made. This could be due to inconsistencies in administration of reagents via micropipettes. This synthesis also had to be performed on a

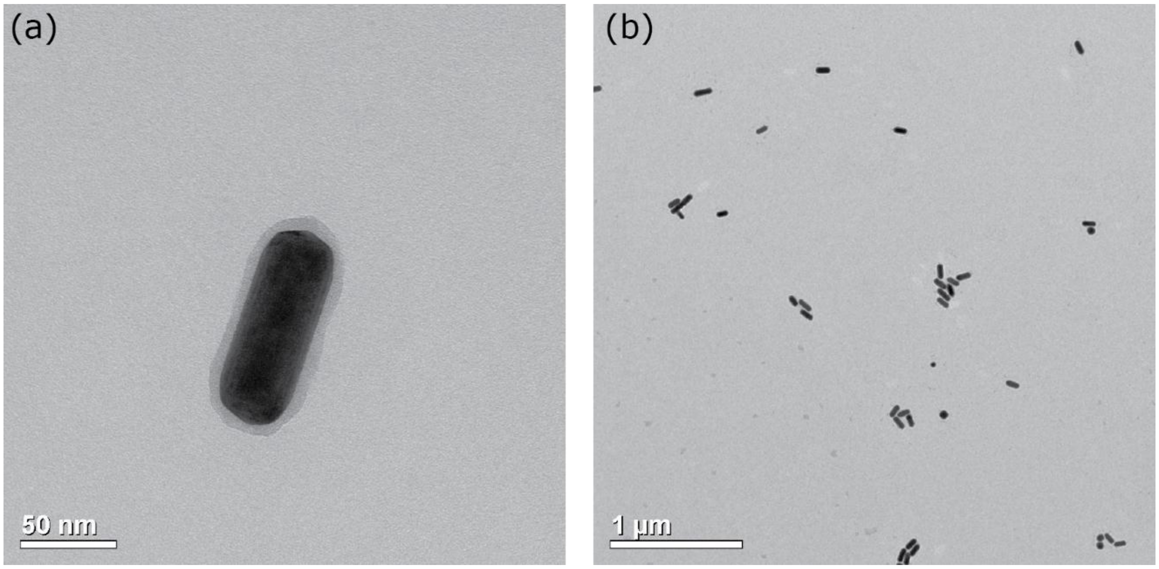

Figure 20: (a) shows a single Au nanorod with a thickness of 5nm synthesized using the procedure by Ye et al. and Wu et al.[67,68] (b) shows a wider area of view of the same particles

small 10 mL scale due to limited Au nanorod stock. This small volume could have magnified any errors introduced by micropipettes.

We next modified the solvent conditions to achieve thinner shells. Work by Wang et al. indicated that the solvent environment can play a large role in the polydispersity and size distribution of silica nanospheres produced via TEOS hydrolysis.[69] This idea led to the hypothesis that changing the solvent conditions may lead to synthesis of a thinner shell that may be less sensitive to small changes in concentration. The nanoparticles shown in Fig. 20 were synthesized in a 2:1 V/V ratio of H_2O:EtOH, whereas the procedure published by Wu et al. uses a solvent composed of pure water with a minor amount of methanol introduced from a TEOS stock solution.[68] This technique quickly proved to have the opposite effect as the intended one, producing a large amorphous shell over a number of Au nanorods as shown in Fig. 21.

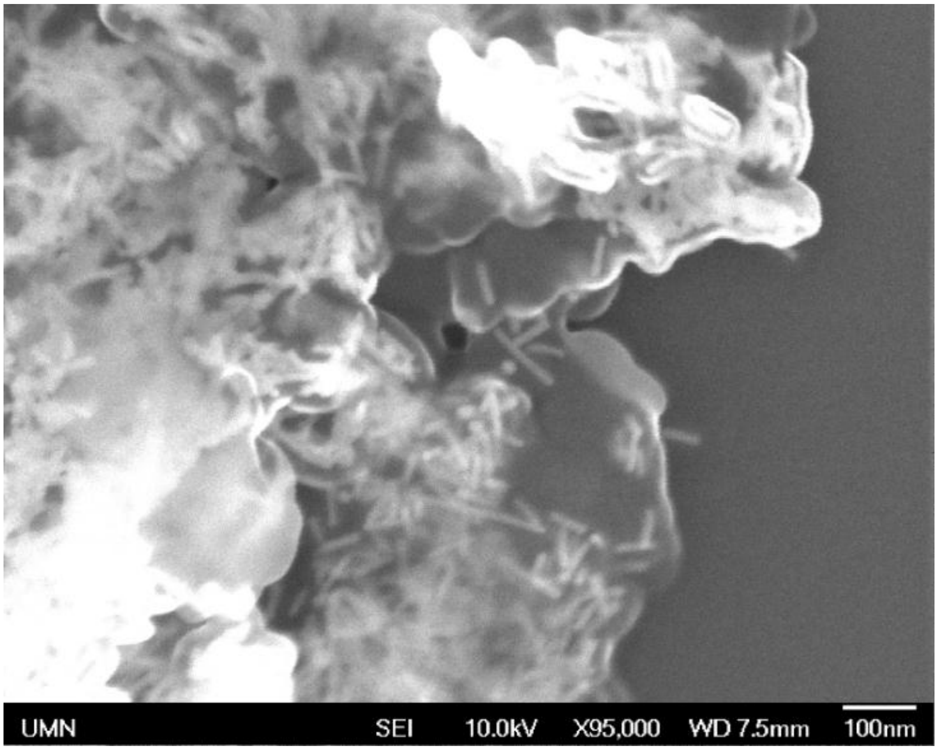

Figure 21: SEM image of silicated Au nanorods synthesized in pure H_2O. Silica completely overgrew into a large amorphous silica mass.

3.5 Formation of Silica Layer: Kozek Synthesis

There are number of possible reasons that these nanorods produced results inconsistent with the procedure published by Wu et al., such as differences in experimental technique, or starting Au nanorod concentration, or in the surface chemistry of the Au nanorods. It is most likely that the difference lies in the Au nanorods. The Au nanorods used by Wu et al. were synthesized using one surfactant CTAB, while our synthesized using a binary surfactant of sodium oleate and CTAB.[56,57] Since the surfactant micelle around the Au nanorod acts a scaffold for the silica growth, this may have changed the way silica growth proceeds. Following this conclusion, the original Au nanorod synthesis used by Wu et al. was synthesized and used as for silication.[57]

The Kozek silication method starts with a more concentrated batch of Au nanorods and is almost identical to the synthesis represented in Figure 18. 18. 50uL of 100mM NaOH, as opposed to ammonium hydroxide, was added to 10ml of pure concentrated Au nanorods to adjust the pH to ~10. 62.5uL 20% v/v TEOS in anhydrous methanol was injected into the Au nanorod solution over 5 minutes while constantly stirring. Following the 30 minutes, 40uL of PEG-Silane was added dropwise over the course of a minute with constant stirring. After 30 minutes the stirring was stopped and held at 30C for 20 hours. The 10ml solution was divided into five 2ml aliquots. Each aliquot was diluted to 40ml, in a 50ml centrifuge tube, with methanol before centrifuging. The silication was halted by centrifuging sample at 8500x*g* for 10 minutes. After 10 minutes, 39ml of supernatant was removed and replaced with fresh methanol. This process was repeated five more times. On the final cycle, the supernatant was removed and the sample was not replaced with methanol. Each of the five samples in centrifuge tubes were recombined into one concentrated solution of silicated Au nanorods. A scheme for this synthesis is shown in Fig. 22.

The silication was successful and thin shells were much more easily achievable after replacing the nanorods. TEM results of the Au nanorods with a 5 nm thickness are shown in Fig. 22.

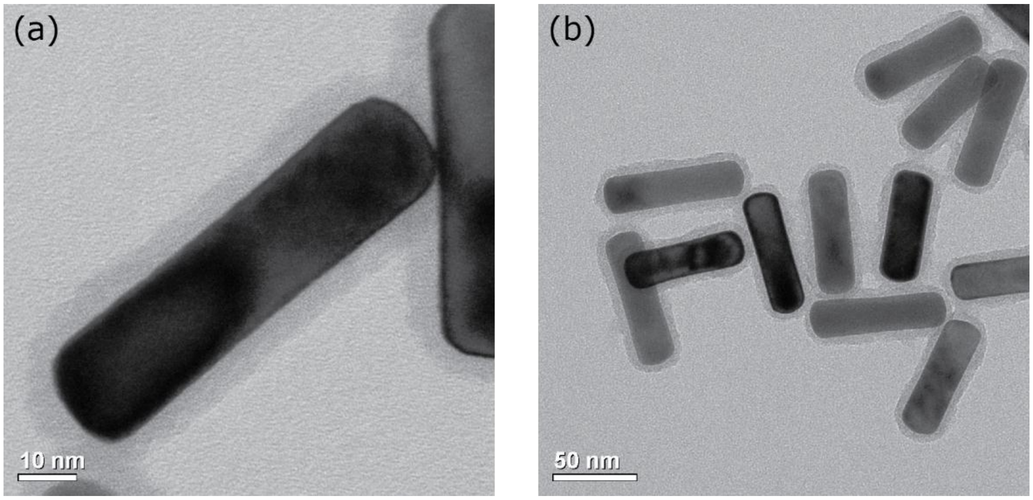

Figure 22: (a) TEM image of Au nanorod synthesized using procedure developed by Kozek et al. and silicated using the procedure developed by Xiu et al. [57,68] (b) shows a larger view over multiple rods of the same batch.

These nanorods were synthesized to yield 10ml of nanorods 45x more concentrated than the previous synthesis, giving us a large supply to be used for self-assembly with Pd nanocubes.

3.6 Silica Cross-Linking

It is worth noting that many of the TEM images of silicated Au nanorods indicated a significant presence of cross linking. An example of this cross-linking is seen in Fig. 23.

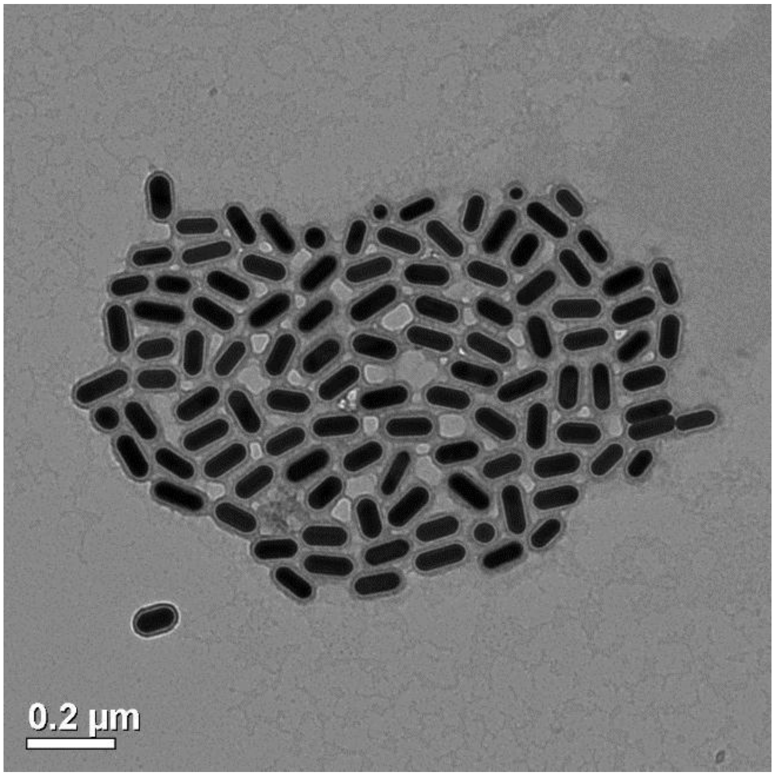

Figure 23: TEM image of 15nm silicated Au nanorods using synthesis by Ye et al. Image appears to show cross-linking of silica between neighboring rods.

This was a significant area of concern as any cross-linking would hinder self-assembly with single particles of Pd cubes, and make dark-field imaging dimers impractical. Although TEM images are useful, observing nanoparticles on a TEM may not be an accurate representation of what is occurring in situ. With this in mind, the claim that the silicated Au nanorods are cross silicated in solution cannot be made simply from looking at the TEM image. UV-VIS can give some insight into the particles in-situ by looking at the spectral width of the surface plasmon resonance, while this can give qualitative information on the polydispersity and presence of aggregates, we needed more quantitative evidence to come a more definitive conclusion about the state of our Au nanorods in solution. To gain more information, solution-state measurements were taken via dynamic light scattering (DLS). DLS is a technique that measures the intensity of light scattered off a colloidal dispersion to determine a size distribution of the particles. The resulting scattering intensity in solution is then used to calculate the diffusion rates of the particle distribution. Given the fluid properties (i.e. temperature, viscosity), the hydrodynamic radius can be calculated.[70] Although the true radius is calculated for spherical particles, the hydrodynamic radius calculated for ellipsoidal particles (rods) needs to be interpreted with caution. The silicated Au nanorods have two primary degrees of freedom: the translational motion of the rod through solution, and the rotation about the transverse axis. Both of these motions will contribute to the way the particle scatters light in solution, and affect the calculated hydrodynamic radius. These radii recorded are not the true hydrodynamic radii of the rod. Nonetheless, based on work done by Glidden et al., we made the assumption that the peak value calculated is within 10-20% of the true length of the rod.[71] Figure 24 shows the corresponding size distribution corresponding to the solution analyzed in Fig. 23.

As seen in Fig. 24, the largest measured hydrodynamic radius was approximately 150 nm. Based on TEM images, the length of the silicated rods are approximately 120nm. The cross-linked Au nanorods in the TEM photograph shown in Fig. 23 is approximately 1400 nm. Since there is no evidence of colloidal particles in that order of magnitude, it is unlikely that significant cross-silication occurred in solution. It is likely that the cross-silication seen in the TEM image is a drying artifact. After the silication is complete, the droplet drying on the TEM grid is concentrates any solvent present in solution. It is possible that the drastic increase in CTAB concentration may have caused some cross-silication on the TEM grids with neighboring particles. Since all CTAB is removed from the solution to prepare rods for self-assembly, this is ultimately not a concern.

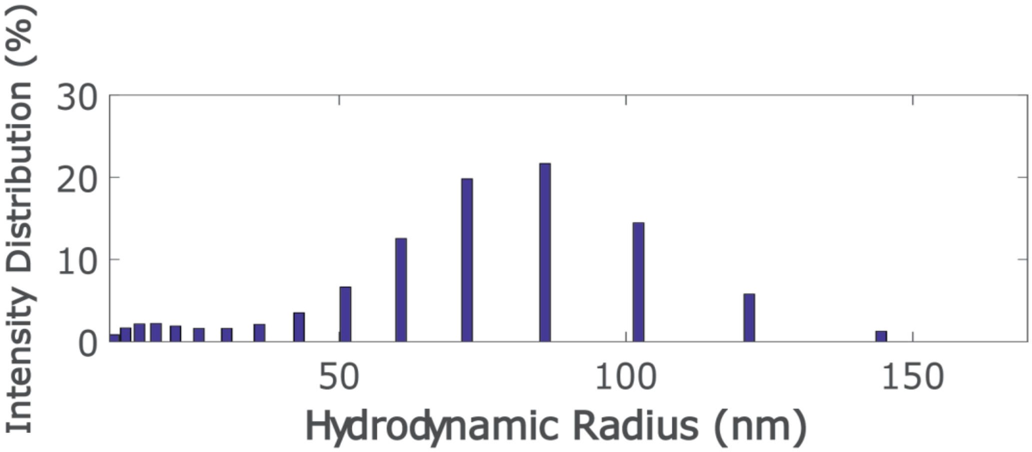

Figure 24: DLS plot shows the percentage of recorded particles at a certain hydrodynamic radius solution analyzed in Figure 23.

3.7 Pd Cube Synthesis

The synthesis of Pd cubes is also a seed-growth synthesis that uses CTAB as a the template developed by Niu et al.[72] First a growth solution of 20 nm seeds are synthesized. To begin, 0.1773 grams of $PdCl_2$ is place in 10 ml of 0.2M HCl. The solution is stirred until crystals are dissolved. After completely dissolved, the solution is diluted to 100ml with MH_2O. This creates an aqueous solution of H_2PdCl_2 at 10mM. To prepare the seeds, 1ml of the H_2PdCl_2 solution is added to 20ml of 12.5mM CTAB solution. The solution is heated to 95C in a water bath controlled using a glass covered thermocouple in solution. A reflux condenser is attached to the solution to ensure any evaporation of solvent reenters the solution. When the solution reaches 95C, 160uL of 100mM L-ascorbic acid is added to the solution. The solution is allowed to stir for 20 minutes, before being added to the growth solution. The growth solution is prepared similarly to the seeds. 19ml of a 50mM CTAB solution is and brought to 60C. 475uL of H_2PdCl_2 solution is added and 304uL of seeds (the seed and CTAB concentration will vary depending on the desired cube size). 190uL of 100mM L-ascorbic acid solution is added to the solution to begin growth. The solution is held at 60C for 2 hours. After completed, the solution is submerged in an ice-bath to halt any further growth. The solution is centrifuged and 18ml of supernatant is removed and replaced with MH2O. The centrifuging process is repeated 2 more times. On the last centrifuge, the supernatant is not replaced with water, but a CTAB stock solution of desired concentration. This will ensure Pd cube concentration is controlled for self-assembly steps.

A graphical scheme of the process is shown in Fig. 25.

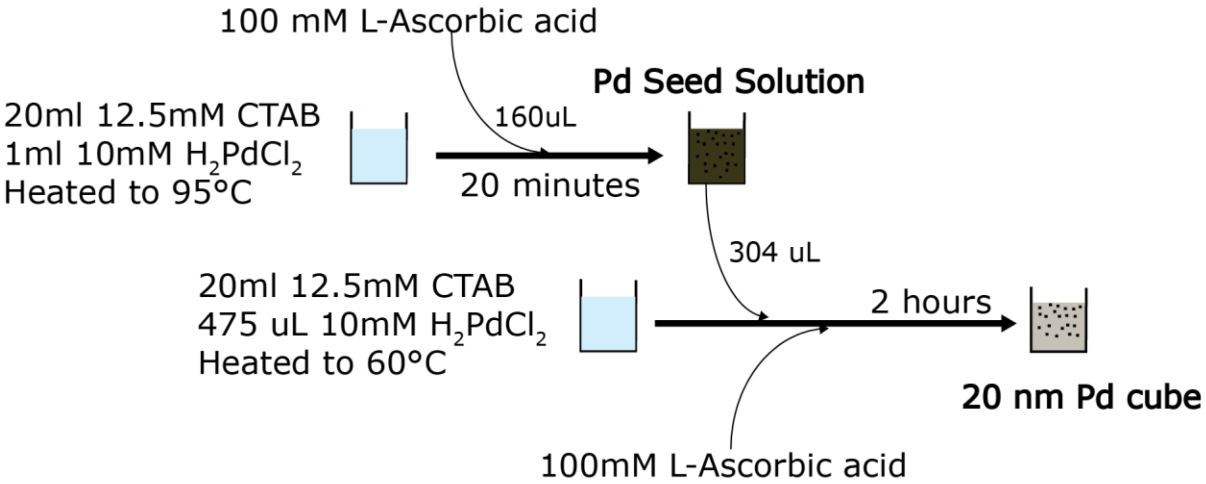

Figure 25: Top section shows the process of creating Pd seeds. These seeds are added to a separate growth solution shown in the bottom section to grow 20nm Pd cubes.

3.8 Self-Assembly Preparation

Although the Au nanorods were silicated, changes still had to be made to the surface to self-assemble dimers with Pd. The zeta potential of a bare silica surface is approximately -40 mV near neutral pH.[73] The Pd cubes are synthesized in CTAB, which results in a zeta-potential of approximately 50 mV.[52] These opposite surface charges make silicated Au nanorods and Pd cubes ideal candidates for electrostatic self-assembly. During the silication, CTAB forms around the Au nanorods, but is also present in solution. Because of this, the ammonium head group is attracted to the free oxygen bond dangling off the nanoparticle surface. This ultimately passivates the silica surface leading to a positive zeta potential. A scheme of a passivated silicated Au nanorod right after silication is seen in Fig. 26.

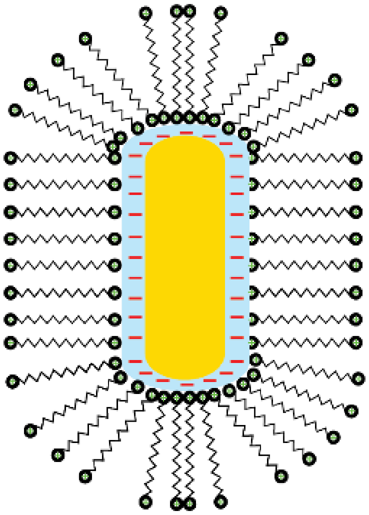

Figure 26 Diagram of CTAB micelle formed around the silicated surface of the Au nanorod. The positively charged CTAB ammonium cation (in green) passivates the negatively charged surface (in red).

In order for the silicated Au nanorods to self-assemble with Pd nanocubes, this passivating CTAB layer must be removed. One method to remove CTAB is using a method developed by Lang et al. to perform an ion exchange using ethanolic ammonium nitrate solution to remove the CTAB off the silica surface.[74] Upon application of ammonium nitration, the ammonium cation from ammonium nitrate exhibits preferential binding to the silica surface, and exchanges with the ammonium cation bound to CTAB. Subsequently, the CTAB becomes displaced in solution and is removed via centrifugation.

Following CTAB removal, the self-assembly process is straightforward. Since the Pd cubes are already functionalized with CTAB after the synthesis is performed, the negatively charged silica of the Au nanorod is exposed and will bind to the Pd cube. Figure 27 shows a scheme of the entire removal and self-assembly process.

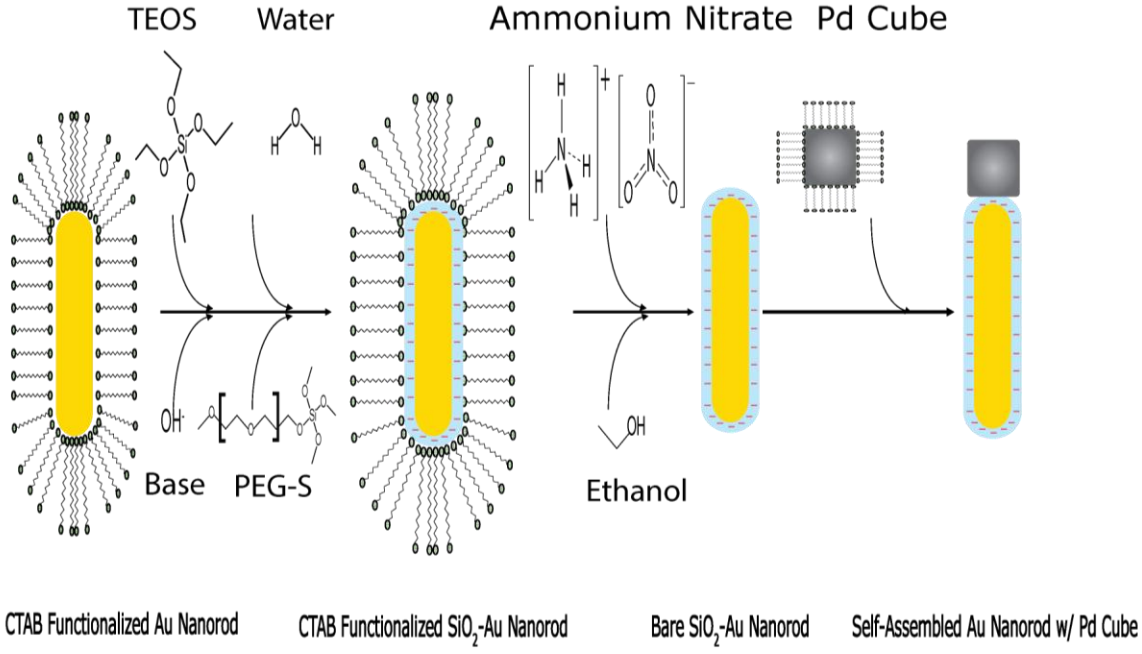

Figure 27: A scheme of the self-assembly process starting from the silication of Au nanorods to removal CTAB layer via ammonium nitrate, and finally self-assembly with a CTAB function Pd cube.

A TEM photograph of a successfully self-assembled Au nanorod and Pd nanocube is seen in Fig. 28.

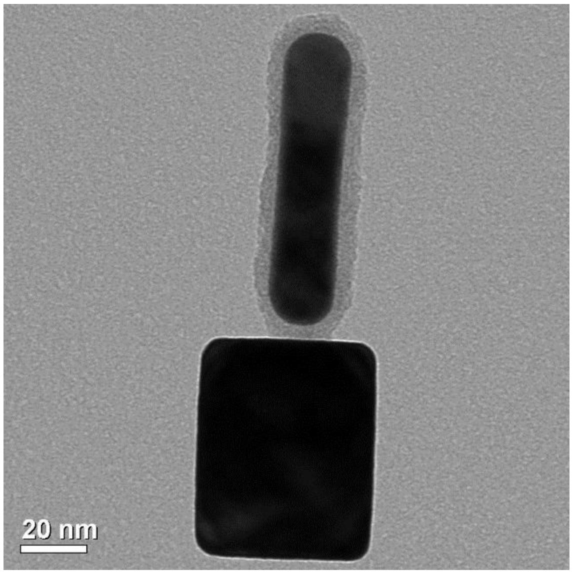

Figure 28: TEM image of Au nanorod with 5nm shell thickness self-assembled with 70nm Pd nanocube.

4 Self-Assembly and Dark-Field Spectroscopy

4.1 Self-Assembly Experiments

After completing the self-assembly preparation for the Au nanorods, self-assembly was performed by combining bare silica-Au nanorods with CTAB functionalized Pd nanocubes. The nanoparticles were combined in different ratios and different CTAB concentrations to change the degree that the silicated Au nanorods and Pd cubes are self-assembled. Figure 29 shows a TEM image of bare Au nanorods self-assembled in a 2:1 ratio at 67uM CTAB.

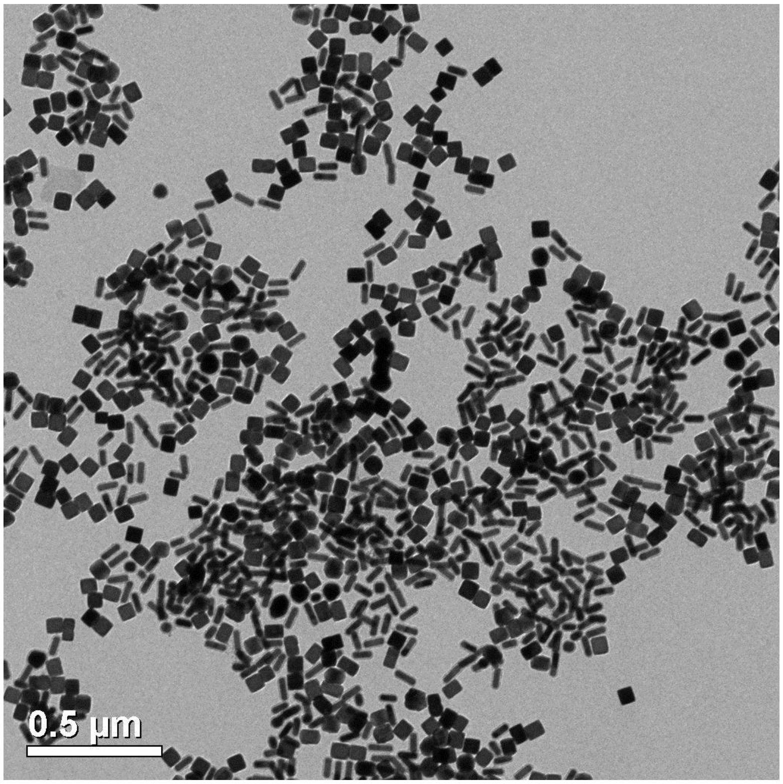

Figure 29: TEM image of 70nm Pd cubes self-assembled 70nm Au nanorods resonant at 738nm.

We assembled the Au nanorods with 70nm cubes as we believed this would give is a larger change in the peak plasmon resonance under hydrogenation. If any single-particle measurements are to be made, then sufficient space, must be given to the particles. We then attempted to self-assemble the particles with Pd cubes at various CTAB concentrations to test its influence on particle distance and self-assembly. Figure 30 shows the effect of changing CTAB concentration.

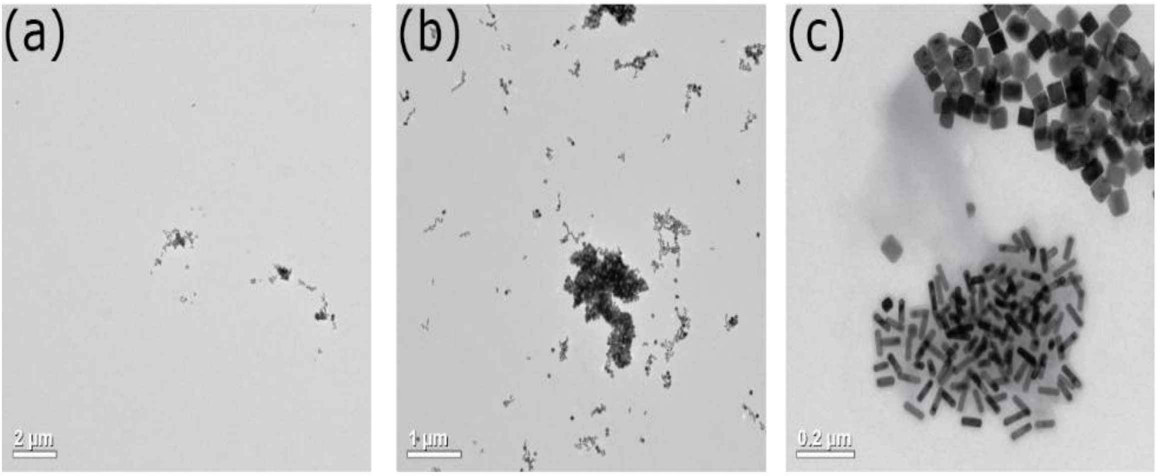

Figure 30: a-c shows the results self-assembling 70nm Au nanorods and 70nm Pd cubes with 2:1 with CTAB concentration of 33uM, 50uM, and 1000uM respectively.

Changing the CTAB concentration does seem to affect the spreading of the particles, but not to a significant degree. In addition, aggregation of particles is still significant. Once a certain threshold of CTAB concentration is reached, the Au nanorods and Pd cubes begin to aggregate and no longer self-assemble as seen in Fig. 30 (c).

The close proximity of the particles is an artifact of the drying of the solution droplet on the TEM grid, and interparticle interactions from the Au nanorods to Pd cubes. One drying effect that occurs in TEM drying known as the “coffee ring effect”. The coffee ring effect describes the buildup of colloidal particles in areas of slower evaporation.[75] Another effect is known surface dewetting where small droplets will form out of the large droplets upon evaporation.[76] A method developed by Michen et al. attempts to mitigate

TEM drying effects by adding Bovine Serum Albumin.[77] Bovine Serum Albumin is a protein that functionalizes the silicated Au nanorod surface adding steric stabilization to the particle, helping prevent aggregation of the particles. In addition, BSA also induces surface tension gradients in the fluid that induces convection to aid in remixing of the particles.[78] BSA also helps in the wetting of the droplet to maximize the interfacial area between the droplet and TEM grid. We attempted to see the effect of adding BSA to silicated Au nanorods at various concentrations by mixing 1ml aliquots of Au nanorod with different volumes of BSA at 1.5mg/ml. The resulting TEM images are seen in

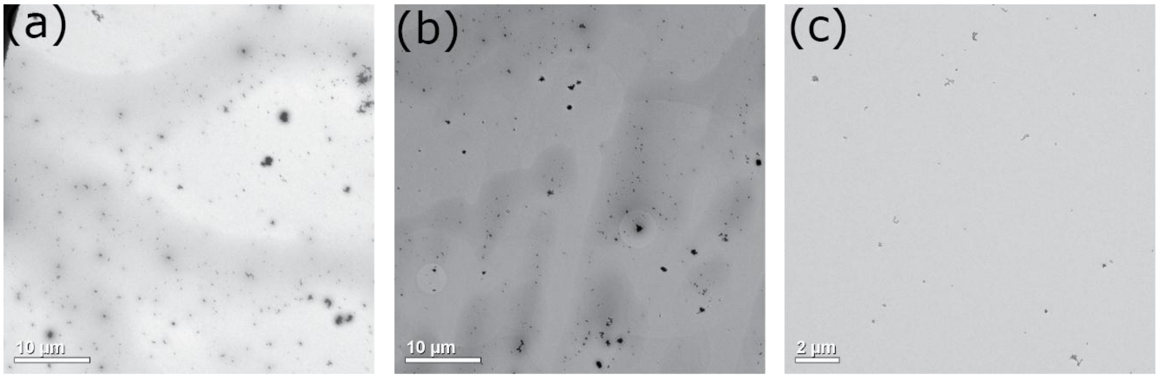

Figure 31: a-c show images of bare silicated Au nanorods mixed with 200 ug/ml, 300 ug/ml, and 400 ug/ml respectively.

As seen in Fig. 31, there does appear to be a spreading effect from the addition of BSA, but it does not appear to have a large number of nanorods in isolation regardless of BSA concentration. We believe that the BSA may be unable to give completely uniform coverage around the Au nanorod. This could mean that certain areas on the Au nanorods are preferentially attracted to other open areas on other Au nanorods. Based on close-up images of Au nanorods, it would appear that this preferential binding is occurring near the tips of the Au nanorods as seen in Fig. 32.

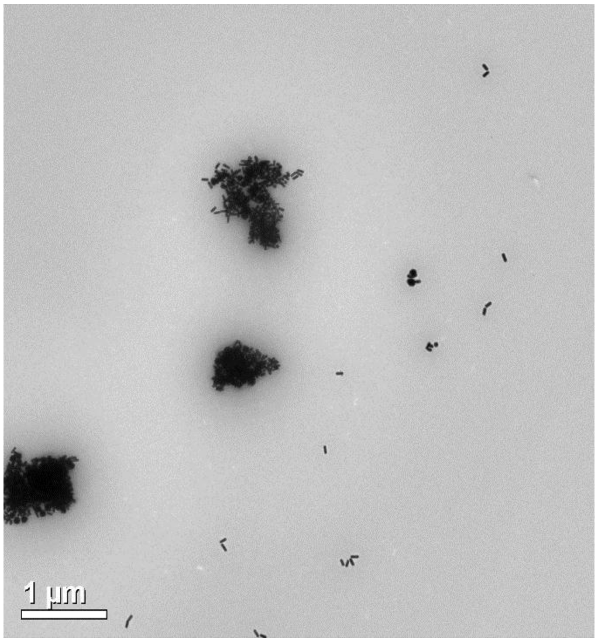

Figure 32: Shows a close up TEM image of bare-silicated Au nanorods with BSA at 400 ug/ml showing preferential binding of Au nanorods near the tips.

Based on the evidence shown, we've been able to successfully self-assemble the Pd cubes with Au nanorods, but the controllability has proven challenging. It's likely that the ellipsoidal shape of the Au nanorods are preventing the BSA from fully increasing the steric hindrance between particles. The majority of particles tested by Michen et al where isotropic in shape, so it's possible that introducing spherical plasmonic reporters may yield better results.[77] A possible synthesis, and self-assembly scheme of using silica-Au-silica core-shell-shell nanoparticles is described in the next section.

4.2 Dark-Field Microscopy Experiments

An inverted optical microscope (Zeiss Axio Observer) set-up used to image nanoparticle samples is shown in Fig. 33. The collected light was coupled into a spectrometer and CCD camera to record spectra of isolated nanoparticles.

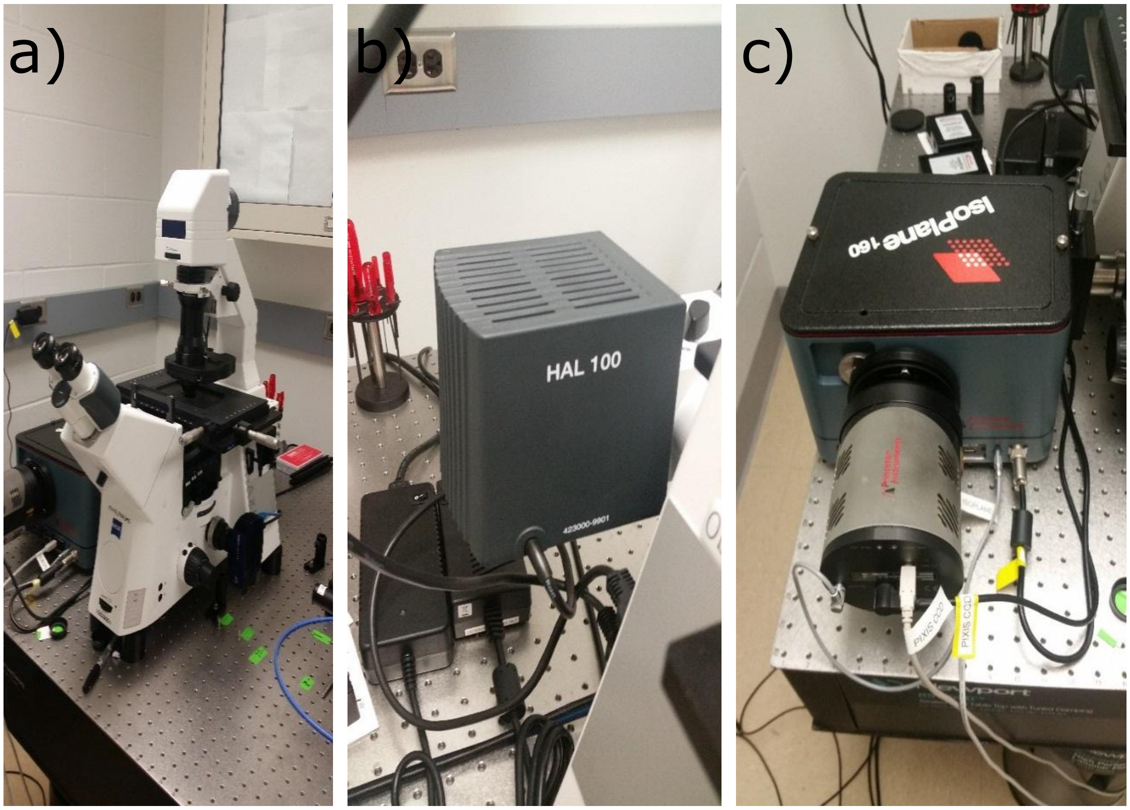

Figure 33: (a) shows the Zeiss Axio Observer 5m used to view nanoparticles. (b) shows the Zeiss Hal 100 Lamp used to illuminate the sample. (c) shows the Princeton Instrument IsoPlane 160 imaging spectrometer with a Princeton Instruments Pixis CCD attached to the back.

In order to utilize dark-field spectroscopy with TEM grids, a specialized holder was fabricated to allow the TEM grid to be supported over the objective while allowing light to scatter off the sample. Figure 34 shows an image of the 3D printed TEM holder.

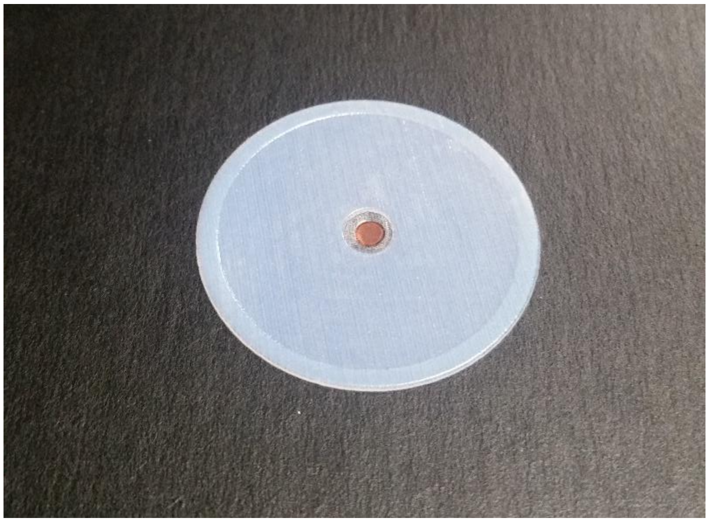

Figure 34: Tem holder that sits on dark-field microscope stage with TEM grid placed in center. Indentation in the middle is 50 microns thick to ensure TEM grid is within the working distance of the objective lens. The length of TEM grid is 4 inches.

We attempted to take scattering spectra of self-assembled 70 nm Au nanorods with 70nm Pd cubes on TEM grids first. The TEM samples that were placed in the dark-field microscope had a few issues. The primary issue had to do with the scattering off the copper mesh on the TEM grids. The large scattering is seen clearly in Fig. 35.

The large scattering from the copper support wires oversaturated the spectrometer, making any signal from the nanoparticles unmeasurable. In addition, significant aggregation of self-assembled nanoparticles on the TEM made finding single particles challenging. The TEM grid is also not completely level due to its flexibility. This also makes it challenging to get a clear image, as the focal plane between the objective lens and the TEM grid changes across the surface.

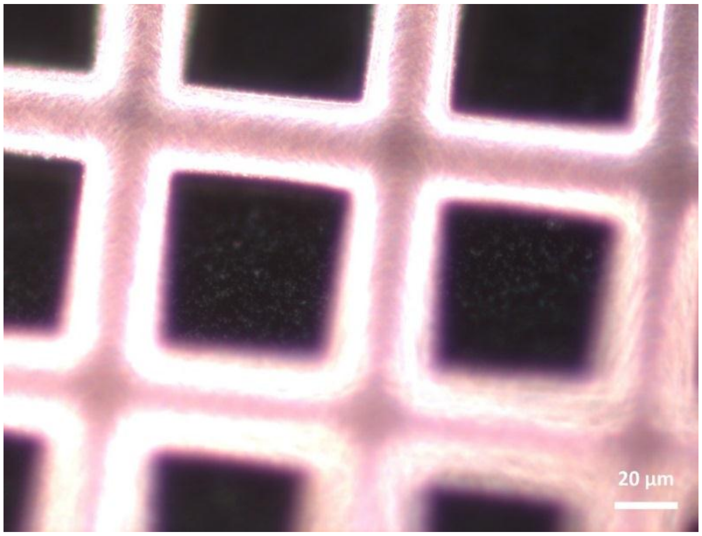

Figure 35: Dark-field image Au nanorods self-assembled with Pd cubes. The large bright cross-hatches are from the copper support wires on the TEM grids.

We then attempted to take a scattering spectrum using only silicated Au nanorods on a glass substrate. These Au nanorods are resonant in the near-Infrared. Figure 36 shows a scattering spectrum of a Au nanorod taken in the dark-field microscope.

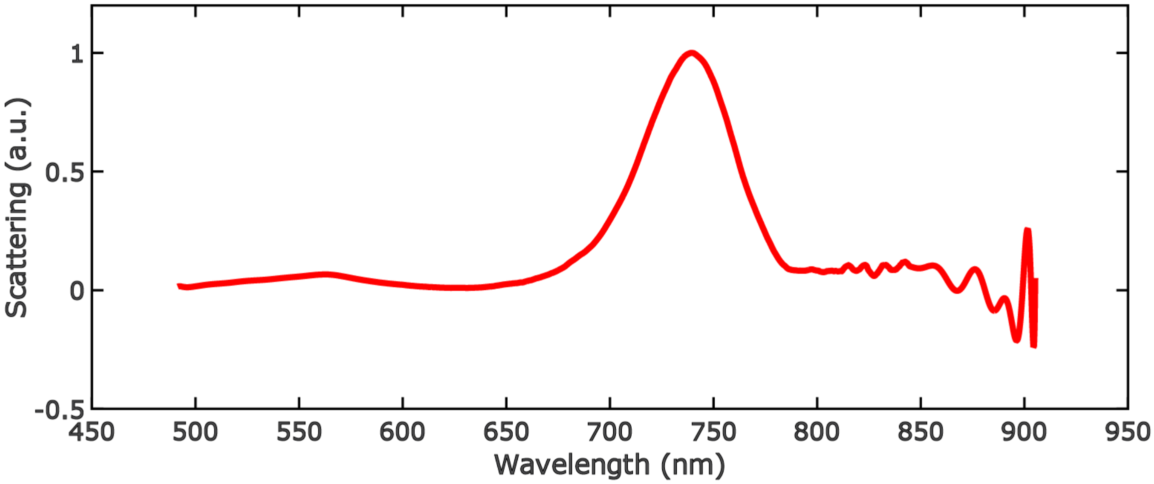

Figure 36: Scattering spectrum of Au nanorod with a longitudinal resonant mode located at 739mn and the transverse resonant mode located at 562nm. The sample was exposed with the halogen-tungsten lamp at 6 volts. The slit width on the spectrometer was 15nm with and exposure time of 4 minutes.

This scattering spectrum of the Au nanorod proved insightful. We were able to see single nanoparticles and see a spectrum that we expected. The presence of the slight increase in scattering intensity at 562 nm is indicative of the transverse localized surface plasmon mode of a Au nanorod, providing further evidence that this is likely a single Au nanorod. One interesting aspect of this spectrum is the noise that appears at around 800 nm. This noise makes scattering spectra of nanoparticles farther into the infrared much less reliable. The cause of this noise is still unclear, but we believe our spectrometer may be receiving secondary reflections that may be causing extra noise in the near-infrared portion of the spectrum. [79] Inserting a long-pass filter at 600 nm may prevent lower wavelength photons from entering the spectrometer and may alleviate this noise.

5 Conclusions and Future Work

5.1 *Developing Silica-Au-Silica Nanoparticles*

Silica-Au-silica core-shell-shell (SGS) nanoparticles are alternative potential candidates for use as plasmonic sensors. The SGS nanoparticle is similar to a silica-Au core-shell nanoparticle , but it has an extra layer of silica wrapping the Au shell.[80] The benefit of using this nanoparticle is that the nanoparticle may show better separation from neighboring particles functionalized with BSA.

The SGS nanoparticles can be synthesized by a method adapted from Xu et al.[81] The synthesis begins by creating the silica cores using the Stober microemulsion method.[82] A reaction mixture of of MH_2O, TEOS, NH_4OH, 3-aminopropyltrimethoxysilane (APTES), and of EtOH is mixed to make the silica cores .[81,83] A solution to prime the growth of the Au shell on the silica cores, known as a Duff Solution, is reduces the Au ions in solution to create 4 nm Au spheres. These Au seeds will functionalize the silica cores to prime the surface further for reduction of Au and subsequent Au shell formation. [84] Separately, the shell growth solution of $HAuCl_4$ is mixed with a K_2CO_3 solution for the gold shell growth solution. The concentrated Au-primed silica-cores are dispersed in this growth solution, and reduced using a NH_2OH solution. The final silica layer is then formed the same way as the original Stober synthesis. When the functionalization of silica around the Au shell is complete, no ligand is functionalized on the surface, so no extra modification will be needed to prepare sample for self-assembly. A scheme of this synthesis and self-assembly is shown in Fig. 37.

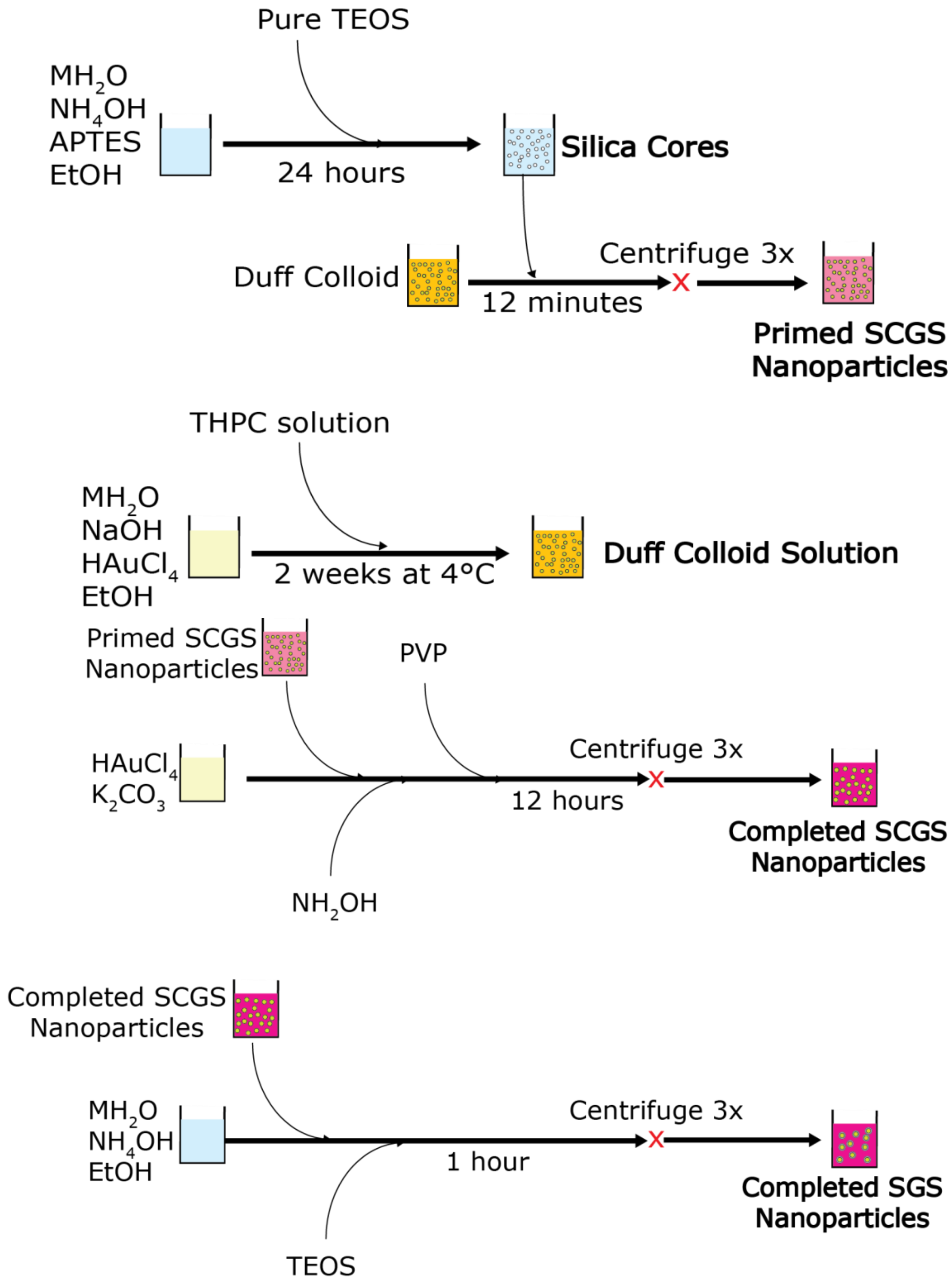

Figure 37: Top half Synthesis scheme for formation of nanoseed primed SCGS (silica-Au core-shell) nanoparticles. Bottom half shows the synthesis of full Au shell SCGS nanoparticles used in making SGS (Silica-Au-Silica core-shell-shell) nanoparticles.

5.2 Alternative Substrates

Given the scattering issues that have been associated with the TEM grids and low working distance, it may be more practical to use a silicon substrate with a 50 nm alumina thin film deposited on the surface using ALD. This would prevent any coupling with the Au-nanoparticles and the silicon substrate. In addition, tracking indicators can be laser etched into the substrate so that images from the SEM can be referenced in the microscope. The use of a flat substrate circumvents the need for a TEM holder, and working distance is not an issue as there is no obstructions separating the nanoparticles from the objective lens. Silicon substrates are also much less fragile than TEM grids and are much less likely to tear. The substrate would then be analyzed in a Scanning Electron Microscope (SEM) over a TEM. An SEM image of self-assembled Pd cubes with silicated Au nanorods is shown in Fig 38.

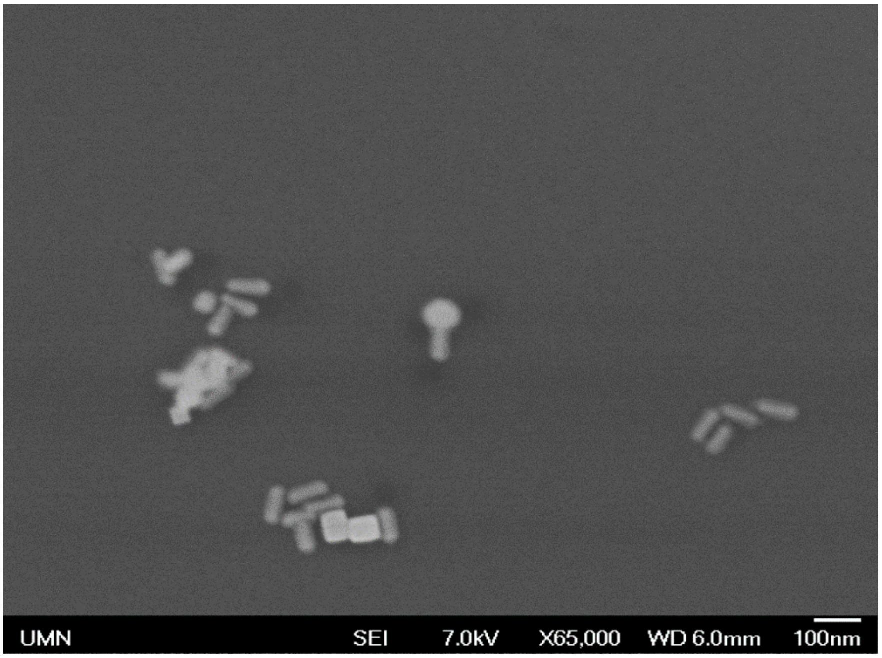

Figure 38: SEM of silicated Au nanorods self-assembled with Pd cubes on a silicon substrate.

5.3 Ellipsometry

Once hydrogenated systems are recorded, the experimental results will need to be validated simulations. The most likely source of error in the simulations comes from the accuracy of the refractive index data and from the roughness associated with the Au. The refractive index data used from Johnson and Christy has proven to agree well with experimental scattering data[85,86]. Our refractive index for Pd and PdH was taken from a 10nm thick Pd thin film.[40] There may be a differences in refractive index between Pd nanocubes of different sizes and this data. Performing spectroscopic ellipsometry on a film of Pd cubes may produce refractive index information closer to that of a single Pd nanoparticle. To do this, a film of Pd nanocubes can be easily formed by drop-casting the solution on a glassy carbon substrate and let to air dry.[87]

The other source of error is related to with the surface roughness on Au. The use of the Duff Colloid adds roughness to the Au shell. In literature, surface roughness on Au has been shown to significantly change the optical response compared to a smooth shell.[80,88] A smooth glass substrate could be functionalized with PVP and attached silica-Au core shells via drop-casting. Subsequently, Using the Tencor P10 profilometer in the Characterization Facility at the University of Minnesota may provide more insight into the surface roughness of the Au. Inspired by a technique utilized by Ferry et al. to characterize textured solar cells, this information could be exported as CAD drawing, and imported to an FDTD solver for more accurate modeling. [89]

5.4 Conclusion

The notion of using plasmonic sensors to detect changes in metallic structures has been a growing interest in the scientific community. How to design plasmonic sensors to detect changes in single nanoparticles is an area that has not been as well explored. As a result of this work, we demonstrate a strong background in the governing aspects behind a plasmonic sensor's ability to detect changes in single, neighboring metallic nanoparticles. Preliminary considerations for designing plasmonic nanoparticles to sense Pd indicate that creating a plasmonic sensor resonant in the near-infrared may allow for a stronger shift in plasmon resonance of the sensor than a sensor resonant at a lower wavelength. We have also shown a heterogenous self-assembly technique for combining silicated Au nanorods and Pd cubes that can be applied to similar systems. Self-assembling heterogeneous nanoparticles with a silicated surface is possible, but may not be practical for asymmetrical particles such as nanorods. Ultimately, this work demonstrates that there is not a one-size-fits-all approach to designing a plasmonic sensor, and that material of interest must be considered before fabrication.

References

1. Giannini, V., Fernández-Domínguez, A. I., Heck, S. C. & Maier, S. A. Plasmonic nanoantennas: fundamentals and their use in controlling the radiative properties of nanoemitters. *Chem. Rev.* **111,** 3888–912 (2011).
2. Alivisatos, P. Semiconductor Clusters, Nanocrystals, and Quantum Dots. *Science (80-.).* **271,** 933–937 (1996).
3. Bohren, C. F. & Huffman, D. R. *Absorption and Scattering of Light by Small Particles*. (Wiley-VCH, 1998).
4. Maier, S. A. & Stefan Alexander Maier. *Plasmonics: Fundamentals and Applications*. (Springer, 2007).
5. Oldenburg, S. ., Averitt, R. ., Westcott, S. . & Halas, N. . Nanoengineering of optical resonances. *Chem. Phys. Lett.* **288,** 243–247 (1998).
6. Zayats, A. V. (Anatoly V. . & Maier, S. A. *Active plasmonics and tuneable plasmonic metamaterials*. (Wiley, 2013).
7. MacDonald, K. F., Samson, Z. L. & Zheludev, N. I. Active plasmonics: Current status. in *2009 IEEE LEOS Annual Meeting Conference Proceedings* 77–77 (IEEE, 2009).

doi:10.1109/LEOS.2009.5343460

8. Guo, L. *et al.* Strategies for enhancing the sensitivity of plasmonic nanosensors. *Nano Today* **10,** 213–239 (2015).
9. Huiberts, J. N. *et al.* Yttrium and lanthanum hydride films with switchable optical properties. *Nature* **380,** 231–234 (1996).
10. Schuller, J. A. *et al.* Plasmonics for extreme light concentration and manipulation. *Nat. Mater.* **9,** 193–204 (2010).
11. Nordlander, P. *et al.* Plasmon Hybridization in Nanoparticle Dimers. *Nano Lett.* **4,** 899–903 (2004).
12. Meier, M. & Wokaun, A. Enhanced fields on large metal particles: dynamic depolarization. *Opt. Lett.* **8,** 581 (1983).
13. Hu, M., Wang, X., Hartland, G. V, Salgueiriño-Maceira, V. & Liz-Marzán, L. M. *Heat dissipation in gold–silica core-shell nanoparticles*. *Chemical Physics Letters* **372,** (2003).
14. Stahelin, R. V. Surface plasmon resonance: a useful technique for cell biologists to characterize biomolecular interactions. *Mol. Biol. Cell* **24,** 883–886 (2013).
15. Robelek, R. Surface plasmon resonance sensors in cell biology: basics and application. *Bioanal. Rev.* **1,** 57–72 (2009).

16. Liedberg, B., Nylander, C. & Lunstr?m, I. Surface plasmon resonance for gas detection and biosensing. *Sensors and Actuators* **4,** 299–304 (1983).

17. and, N. N. & Chilkoti*, A. A Colorimetric Gold Nanoparticle Sensor To Interrogate Biomolecular Interactions in Real Time on a Surface. (2001). doi:10.1021/AC015657X

18. Khanna, V. K. *Nanosensors : physical, chemical, and biological*. (Taylor & Francis, 2011).

19. Strobbia, P., Languirand, E. & Cullum, B. M. Recent advances in plasmonic nanostructures for sensing: a review. *Opt. Eng.* **54,** 100902 (2015).

20. Li, Z. *et al.* Boosting figures of merit of cavity plasmon resonance based refractive index sensing in dielectric-metal core-shell resonators. *Opt. Express* **24,** 19895 (2016).

21. Yguerabide, J. & Yguerabide, E. E. Light-Scattering Submicroscopic Particles as Highly Fluorescent Analogs and Their Use as Tracer Labels in Clinical and Biological Applications. *Anal. Biochem.* **262,** 157–176 (1998).

22. Colleen L. Nehl, †, Hongwei Liao, ‡ and & Jason H. Hafner*, †,‡.

Optical Properties of Star-Shaped Gold Nanoparticles. (2006). doi:10.1021/NL052409Y

23. Bévenot, X., Trouillet, A., Veillas, C., Gagnaire, H. & Clément, M. Surface plasmon resonance hydrogen sensor using an optical fibre*. *Meas. Sci. Technol.* **13,** 118–124 (2002).

24. Yoshimura, K., Langhammer, C. & Dam, B. Metal hydrides for smart window and sensor applications. *MRS Bull.* **38,** 495–503 (2013).

25. Tittl, A. *et al.* Plasmonic Smart Dust for Probing Local Chemical Reactions. *Nano Lett.* **13,** 1816–1821 (2013).

26. Langhammer, C., Larsson, E. M., Kasemo, B. & Zorić, I. Indirect Nanoplasmonic Sensing: Ultrasensitive Experimental Platform for Nanomaterials Science and Optical Nanocalorimetry. *Nano Lett.* **10,** 3529–3538 (2010).

27. Liu, N., Tang, M. L., Hentschel, M., Giessen, H. & Alivisatos, A. P. Nanoantenna-enhanced gas sensing in a single tailored nanofocus. *Nat. Mater.* **10,** 631–636 (2011).

28. Schlapbach, L. & Zuttel, A. Hydrogen-storage materials for mobile applications. *Nature* **414,** 353–358 (2001).

29. Li, G. *et al.* Shape-dependent hydrogen-storage properties in Pd

nanocrystals: Which does hydrogen prefer, octahedron (111) or cube (100)? *J. Am. Chem. Soc.* **136,** 10222–10225 (2014).

30. Syrenova, S. *et al.* Hydride formation thermodynamics and hysteresis in individual Pd nanocrystals with different size and shape. *Nat. Mater.* **14,** 1236–1243 (2015).
31. Baldi, A., Narayan, T. C., Koh, A. L. & Dionne, J. A. In situ detection of hydrogen-induced phase transitions in individual palladium nanocrystals. *Nat. Mater.* **13,** 1143–1148 (2014).
32. Manchester, F. D., San-Martin, A. & Pitre, J. M. The H-Pd (hydrogen-palladium) System. *J. Phase Equilibria* **15,** 62–83 (1994).
33. Shen, Y. *et al.* Plasmonic gold mushroom arrays with refractive index sensing figures of merit approaching the theoretical limit. *Nat. Commun.* **4,** 1–9 (2013).
34. Charles, D. E. *et al.* Versatile Solution Phase Triangular Silver Nanoplates for Highly Sensitive Plasmon Resonance Sensing. *ACS Nano* **4,** 55–64 (2010).
35. Jeong, H.-H. *et al.* Dispersion and shape engineered plasmonic nanosensors. *Nat. Commun.* **7,** 11331 (2016).
36. Mayer, K. M. & Hafner, J. H. Localized Surface Plasmon Resonance

Sensors. *Chem. Rev.* **111,** 3828–3857 (2011).

37. Nusz, G. J., Curry, A. C., Marinakos, S. M., Wax, A. & Chilkoti, A. Rational Selection of Gold Nanorod Geometry for Label-Free Plasmonic Biosensors. *ACS Nano* **3,** 795–806 (2009).

38. Svedendahl, M., Chen, S., Dmitriev, A. & Käll, M. Refractometric Sensing Using Propagating versus Localized Surface Plasmons: A Direct Comparison. *Nano Lett.* **9,** 4428–4433 (2009).

39. Offermans, P. *et al.* Universal Scaling of the Figure of Merit of Plasmonic Sensors. *ACS Nano* **5,** 5151–5157 (2011).

40. Rottkay, K. von *et al.* Refractive index changes of Pd-coated magnesium lanthanide switchable mirrors upon hydrogen insertion. *J. Appl. Phys.* **85,** 408–413 (1999).

41. Kasap, S. *Principles of electronic materials and devices*. (McGraw-Hill, 2006).

42. Lumerical Product Overview. at <https://www.lumerical.com/tcad-products/>

43. Min, Y., Akbulut, M., Kristiansen, K., Golan, Y. & Israelachvili, J. The role of interparticle and external forces in nanoparticle assembly. *Nat. Mater.* **7,** 527–538 (2008).

44. Pinheiro, A. V., Han, D., Shih, W. M. & Yan, H. Challenges and opportunities for structural DNA nanotechnology. *Nat. Nanotechnol.* **6,** 763–772 (2011).

45. Dill, K. A. & MacCallum, J. L. The Protein-Folding Problem, 50 Years On. *Science (80-.).* **338,** (2012).

46. Chen, I. A. & Walde, P. From self-assembled vesicles to protocells. *Cold Spring Harb. Perspect. Biol.* **2,** a002170 (2010).

47. Thacker, V. V. *et al.* DNA origami based assembly of gold nanoparticle dimers for surface-enhanced Raman scattering. *Nat. Commun.* **5,** 1–7 (2014).

48. Linda Gunnarsson *et al.* Confined Plasmons in Nanofabricated Single Silver Particle Pairs: Experimental Observations of Strong Interparticle Interactions. (2004). doi:10.1021/JP049084E

49. Björn M. Reinhard, †,‡, Merek Siu, §, Harish Agarwal, †, A. Paul Alivisatos, ∥,⊥ and & Jan Liphardt*, †,‡,§. Calibration of Dynamic Molecular Rulers Based on Plasmon Coupling between Gold Nanoparticles. (2005). doi:10.1021/NL051592S

50. Loweth, C. J., Caldwell, W. B., Peng, X., Alivisatos, A. P. & Schultz, P. G. DNA-Based Assembly of Gold Nanocrystals. *Angew. Chemie*

Int. Ed. **38,** 1808–1812 (1999).

51. Busson, M. P. *et al.* Optical and Topological Characterization of Gold Nanoparticle Dimers Linked by a Single DNA Double Strand. *Nano Lett.* **11,** 5060–5065 (2011).
52. Gschneidtner, T. A. *et al.* A versatile self-assembly strategy for the synthesis of shape-selected colloidal noble metal nanoparticle heterodimers. *Langmuir* **30,** 3041–3050 (2014).
53. Morrison, I. D. & Ross, S. *Colloidal dispersions : suspensions, emulsions, and foams*. (Wiley-Interscience, 2002).
54. Jiang, J., Oberdörster, G. & Biswas, P. Characterization of size, surface charge, and agglomeration state of nanoparticle dispersions for toxicological studies. *J. Nanoparticle Res.* **11,** 77–89 (2009).
55. Bard, A. J. & Faulkner, L. R. *Electrochemical methods : fundamentals and applications*. (Wiley, 2001).
56. Ye, X., Zheng, C., Chen, J., Gao, Y. & Murray, C. B. Using Binary Surfactant Mixtures To Simultaneously Improve the Dimensional Tunability and Monodispersity in the Seeded Growth of Gold Nanorods. *Nano Lett.* **13,** 765–771 (2013).
57. Kozek, K. A., Kozek, K. M., Wu, W.-C., Mishra, S. R. & Tracy, J. B.

Large-Scale Synthesis of Gold Nanorods through Continuous Secondary Growth. *Chem. Mater.* **25,** 4537–4544 (2013).

58. Zhu, J. Shape dependent full width at half maximum of the absorption band in gold nanorods. *Phys. Lett. A* **339,** 466–471 (2005).

59. Zhang, Q. *et al.* Facet Control of Gold Nanorods. *ACS Nano* **10,** 2960–2974 (2016).

60. Niu, W., Zhang, L. & Xu, G. Seed-mediated growth method for high-quality noble metal nanocrystals. *Sci. China Chem.* **55,** 2311–2317 (2012).

61. Lohse, S. E. & Murphy, C. J. The Quest for Shape Control: A History of Gold Nanorod Synthesis. *Chem. Mater.* **25,** 1250–1261 (2013).

62. Burrows, N. D. *et al.* Surface Chemistry of Gold Nanorods. *Langmuir* **32,** acs.langmuir.6b02706 (2016).

63. Mayerhöfer, T. G., Mutschke, H. & Popp, J. Employing Theories Far beyond Their Limits-The Case of the (Boguer-) Beer-Lambert Law. *ChemPhysChem* **17,** 1948–1955 (2016).

64. Scarabelli, L., Sánchez-Iglesias, A., Pérez-Juste, J. & Liz-Marzán, L. M. A ‘Tips and Tricks’ Practical Guide to the Synthesis of Gold Nanorods. *J. Phys. Chem. Lett.* **6,** 4270–4279 (2015).

65. Tang, M. L., Liu, N., Dionne, J. A. & Alivisatos, A. P. Observations of Shape-Dependent Hydrogen Uptake Trajectories from Single Nanocrystals. *J. Am. Chem. Soc.* **133,** 13220–13223 (2011).

66. Zhan, Q. *et al.* A study of mesoporous silica-encapsulated gold nanorods as enhanced light scattering probes for cancer cell imaging. *Nanotechnology* **21,** 55704 (2010).

67. Nguyen, S. C. *et al.* Study of Heat Transfer Dynamics from Gold Nanorods to the Environment *via* Time-Resolved Infrared Spectroscopy. *ACS Nano* **10,** 2144–2151 (2016).

68. Wu, W.-C. & Tracy, J. B. Large-Scale Silica Overcoating of Gold Nanorods with Tunable Shell Thicknesses. *Chem. Mater.* **27,** 2888–2894 (2015).

69. Nghiem, T. H. L. *et al.* Preparation and characterization of silica-gold core-shell nanoparticles. *J. Nanoparticle Res.* **15,** (2013).

70. Berne, B. J. & Pecora, R. *Dynamic light scattering : with applications to chemistry, biology, and physics*. (Dover Publications, 2000).

71. Glidden, M. & Muschol, M. Characterizing Gold Nanorods in Solution Using Depolarized Dynamic Light Scattering. *J. Phys. Chem. C* **116,** 8128–8137 (2012).

72. Niu, W., Zhang, L. & Xu, G. Shape-Controlled Synthesis of Single-Crystalline Palladium Nanocrystals. *ACS Nano* **4,** 1987–1996 (2010).

73. An, S. S. A. *et al.* Surface treatment of silica nanoparticles for stable and charge-controlled colloidal silica. *Int. J. Nanomedicine* **9,** 29 (2014).

74. Natacha, L. & Tuel, A. A Fast and Efficient Ion-Exchange Procedure To Remove Surfactant Molecules from MCM-41 Materials. *Chem. Mater.* (2004). doi:10.1021/CM030633N

75. Deegan, R. D. *et al.* Capillary flow as the cause of ring stains from dried liquid drops. *Nature* **389,** 827–829 (1997).

76. Picknett, R. . & Bexon, R. The evaporation of sessile or pendant drops in still air. *J. Colloid Interface Sci.* **61,** 336–350 (1977).

77. Michen, B. *et al.* Avoiding drying-artifacts in transmission electron microscopy: Characterizing the size and colloidal state of nanoparticles. *Sci. Rep.* **5,** 9793 (2015).

78. Scriven, L. E. & Sternling, C. V. The Marangoni Effects. *Nature* **187,** 186–188 (1960).

79. Li, G.-C., Zhang, Y.-L., Jiang, J., Luo, Y. & Lei, D. Y. Metal-Substrate-Mediated Plasmon Hybridization in a Nanoparticle Dimer

for Photoluminescence Line-Width Shrinking and Intensity Enhancement. *ACS Nano* acsnano.7b00048 (2017). doi:10.1021/acsnano.7b00048

80. Bardhan, R. *et al.* Nanosphere-in-a-Nanoshell: A Simple Nanomatryushka. *J. Phys. Chem. C* **114,** 7378–7383 (2010).

81. Xu, S., Hartvickson, S. & Zhao, J. X. Engineering of SiO2−Au−SiO2 Sandwich Nanoaggregates Using a Building Block: Single, Double, and Triple Cores for Enhancement of Near Infrared Fluorescence. *Langmuir* **24,** 7492–7499 (2008).

82. H. E. Bergna, W. O. R., Bergna, H. E. & Roberts, W. O. Colloidal Silica: Fundamentals and Applications. *Int. J. Numer. Methods Fluids* **41,** 1–1 (2003).

83. Liang, S. *et al.* A Silica–Gold–Silica Nanocomposite for Photothermal Therapy in the Near-Infrared Region. *ACS Appl. Mater. Interfaces* **7,** 85–93 (2015).

84. Duff, D. G., Baiker, A. & Edwards, P. P. A new hydrosol of gold clusters. 1. Formation and particle size variation. *Langmuir* **9,** 2301–2309 (1993).

85. Colleen L. Nehl, † *et al.* Scattering Spectra of Single Gold Nanoshells.

(2004). doi:10.1021/NL048610A

86. Johnson, P. B. & Christy, R. W. Optical Constants of the Noble Metals. *Phys. Rev. B* **6,** 4370–4379 (1972).

87. Chang, G., Oyama, M. & Hirao, K. Facile synthesis of monodisperse palladium nanocubes and the characteristics of self-assembly. *Acta Mater.* **55,** 3453–3456 (2007).

88. Sanchez-Gaytan, B. L. *et al.* Controlling the Topography and Surface Plasmon Resonance of Gold Nanoshells by a Templated Surfactant-Assisted Seed Growth Method. *J. Phys. Chem. C* **117,** 8916–8923 (2013).

89. Vivian Ferry *et al.* Light trapping in thin film plasmonic solar cells. *Proc. 25th EU-PVSEC Conf. Val.* 6–10 (2010).

90. Bleck, W. *Material science of Steel: Textbook for RWTH Students*. (Aachen, 2007).

91. Lewis, F. A. The Hydrides of Palladium and Palladium Alloys | Johnson Matthey Technology Review. *Platin. Met. Rev.* **4,** 132–137 (1960).

92. Israelachvili, J. N. *Intermolecular and surface forces*. (Academic Press, 2011).

93. Yi, Z. *et al.* A New Insight into Growth Mechanism and Kinetics of Mesoporous Silica Nanoparticles by in Situ Small Angle X-ray Scattering. *Langmuir* **31,** 8478–8487 (2015).

Appendix

Table 1: Preliminary simulations showing the extent of the blue shift with changing gap size upon self-assembling a SCGS with a core diameter of 100nm and shell thickness of 10nm. Trend indicates that a gap distance beyond 5nm shows very little blue shift.

Pd Cube Size (nm)	Gap Distance (nm)	Blue Shift (nm)
40	1	7
40	3	3
40	5	2
40	10	0